The influence of magnetic fields in planetary dynamo models

Krista M. Soderlund [a,*], Eric M. King [b], Jonathan M. Aurnou [a]

[a] Department of Earth and Space Sciences, University of California, Los Angeles, CA 90095, USA
[b] Department of Earth and Planetary Science, University of California, Berkeley, CA 94720, USA

ARTICLE INFO

ABSTRACT

The magnetic fields of planets and stars are thought to play an important role in the fluid motions responsible for their field generation, as magnetic energy is ultimately derived from kinetic energy. We investigate the influence of magnetic fields on convective dynamo models by contrasting them with non-magnetic, but otherwise identical, simulations. This survey considers models with Prandtl number $Pr=1$; magnetic Prandtl numbers up to $Pm=5$; Ekman numbers in the range $10^{-3} \geq E \geq 10^{-5}$; and Rayleigh numbers from near onset to more than 1000 times critical.

Two major points are addressed in this letter. First, we find that the characteristics of convection, including convective flow structures and speeds as well as heat transfer efficiency, are not strongly affected by the presence of magnetic fields in most of our models. While Lorentz forces must alter the flow to limit the amplitude of magnetic field growth, we find that dynamo action does not necessitate a significant change to the overall flow field. By directly calculating the forces in each of our simulations, we show that the traditionally defined Elsasser number, Λ_i, overestimates the role of the Lorentz force in dynamos. The Coriolis force remains greater than the Lorentz force even in cases with $\Lambda_i \simeq 100$, explaining the persistence of columnar flows in $\Lambda_i > 1$ dynamo simulations. We argue that a dynamic Elsasser number, Λ_d, better represents the Lorentz to Coriolis force ratio. By applying the Λ_d parametrization to planetary settings, we predict that the convective dynamics (excluding zonal flows) in planetary interiors are only weakly influenced by their large-scale magnetic fields.

The second major point addressed here is the observed transition between dynamos with dipolar and multipolar magnetic fields. We find that the breakdown of dipolar field generation is due to the degradation of helicity in the flow. This helicity change does not coincide with the destruction of columnar convection and is not strongly influenced by the presence of magnetic fields. Force calculations suggest that this transition may be related to a competition between inertial and viscous forces. If viscosity is indeed important for large-scale field generation, such moderate Ekman number models may not adequately simulate the dynamics of planetary dynamos, where viscous effects are expected to be negligible.

© 2012 Elsevier B.V. All rights reserved.

1. Introduction

Magnetic fields are common throughout the solar system; intrinsic magnetic fields have been detected on the Sun, Mercury, Earth, the giant planets, and the Jovian satellite Ganymede (Connerney, 2007). Evidence of extinct dynamos is also observed on the Moon and Mars (Connerney, 2007). In addition, it is expected that many extrasolar planets have magnetic fields (e.g., Gaidos et al., 2010). Planetary magnetic fields result from dynamo action thought to be driven by convection in electrically conducting fluid regions (e.g., Jones, 2011) and, therefore, are linked to the planets' internal dynamics. Convection in these systems is subject to Coriolis forces resulting from planetary rotation. In electrically conducting fluids, these flows can be unstable to dynamo action. Lorentz forces then arise, via Lenz's law, that act to equilibrate magnetic field growth.

Insight into the forces that govern the fluid dynamics of planetary interiors can be gained through numerical modeling: non-magnetic rotating convection models investigate the influence of rotation on convection, and planetary dynamo models incorporate the additional back reaction of the magnetic fields on the fluid motions from which they arise.

The flows in non-magnetic rapidly rotating convection are organized by the Coriolis force into axial columns (e.g., Grooms

* Corresponding author. Present address: Institute for Geophysics, John A. & Katherine G. Jackson School of Geosciences, The University of Texas at Austin, Austin, TX 78758, USA. Tel.: +1 218 349 3006; fax: +1 512 471 8844.
E-mail addresses: krista@ig.utexas.edu,
ksoderlund@gmail.com (K.M. Soderlund), eric.king@berkeley.edu (E.M. King),
aurnou@ucla.edu (J.M. Aurnou).

et al., 2010; Olson, 2011; King and Aurnou, 2012). Under the extreme influence of rotation, the dominant force balance is geostrophic—a balance between the Coriolis force and the pressure gradient. Geostrophic flows are described by the Taylor–Proudman constraint, which predicts that fluid motions should not vary strongly in the direction of the rotation axis (e.g., Tritton, 1998). Furthermore, linear asymptotic analyses predict that the azimuthal wavenumber of these columns varies as $m = \mathcal{O}(E^{-1/3})$ as $E \to 0$ (Roberts, 1968; Jones et al., 2000; Dormy et al., 2004). Here, m is non-dimensionalized by the shell thickness and the Ekman number, E, characterizes the ratio of viscous to Coriolis

forces (see Table 1). Thus, in rapidly rotating systems such as planetary cores (where $E \lesssim 10^{-10}$), it is predicted that convection occurs as tall, thin columns. Flows in these columns are helical, and these corkscrew-like motions are important for large-scale magnetic field generation (e.g., Jones, 2011).

In planetary dynamos, however, magnetic fields are also thought to play an important dynamical role on the convection and zonal flows. It is often argued that the influence of magnetic fields will be important when $\Lambda_i \gtrsim 1$, where the traditional Elsasser number, Λ_i, characterizes the relative strengths of the Lorentz and Coriolis forces (see Table 2). In the presence of dominant imposed magnetic fields and rotation, the first order force balance is magnetostrophic—a balance between the Coriolis, pressure gradient, and Lorentz terms. Studies of linear magnetoconvection show that the azimuthal wavenumber of convection decreases to $m = \mathcal{O}(1)$ when a strong magnetic field ($\Lambda_i \gtrsim \mathcal{O}(1)$) is imposed in the limit $E \to 0$ (Chandrasekhar, 1961; Eltayeb and Roberts, 1970; Fearn and Proctor, 1983; Cardin and Olson, 1995). This behavior occurs because magnetic fields can relax the Taylor–Proudman constraint, allowing global-scale motions that differ fundamentally from the small-scale axial columns typical of non-magnetic, rapidly rotating convection.

Despite having strong magnetic fields, however, axial convective flow structures are maintained in many rotating magnetoconvection and dynamo studies (e.g., Olson and Glatzmaier, 1995; Zhang, 1995; Kageyama and Sato, 1997; Zhang et al., 1998;

Table 1
Summary of non-dimensional control parameters. Symbols are defined in the text. Parameter estimates for Earth's core taken from King et al. (2010).

Definition	Interpretation	Model	Earth's core
$\chi = r_i/r_o$	Shell geometry	0.4	0.35
$Ra = \alpha g_o \Delta T D^3 / \nu\kappa$	Buoyancy/diffusion	$10^5 < Ra < 10^9$	$\sim 10^{24}$
$E = \nu/2\Omega D^2$	Viscous/Coriolis forces	$10^{-3}, 10^{-4}, 10^{-5}$	$\sim 10^{-15}$
$Pr = \nu/\kappa$	Viscous/thermal diffusivities	1	$\sim 10^{-1}$
$Pm = \nu/\eta$	Viscous/magnetic diffusivities	0, 2, 5	$\sim 10^{-6}$

Table 2
Summary of non-dimensional diagnostic parameters. Symbols are defined in the text. In these definitions, $\ell_B = (\pi D/2)/\overline{k_B}$ is assumed to be the characteristic quarter-wavelength of the magnetic field.

Parameter	Definition	Interpretation
	$\mathcal{E}_K = \frac{1}{2V_s}\int \mathbf{u}\cdot\mathbf{u}\,dV$	Kinetic energy density
	$\mathcal{E}_K^c = \mathcal{E}_K - \mathcal{E}_{K,Toroidal}^{Axisymmetric}$	Convective kinetic energy density
	$\mathcal{E}_M = \frac{1}{2V_s}\int \mathbf{B}\cdot\mathbf{B}\,dV$	Magnetic energy density
	$\overline{l_u} = \sum l(\mathbf{u}_l\cdot\mathbf{u}_l)/2\mathcal{E}_K$	Characteristic degree of the flow
	$\overline{l_B} = \sum l(\mathbf{B}_l\cdot\mathbf{B}_l)/2\mathcal{E}_M$	Characteristic degree of the **B** field
	$\overline{m_u} = \sum m(\mathbf{u}_m\cdot\mathbf{u}_m)/2\mathcal{E}_K$	Characteristic order of the flow
	$\overline{m_B} = \sum m(\mathbf{B}_m\cdot\mathbf{B}_m)/2\mathcal{E}_M$	Characteristic order of the **B** field
	$\overline{k_u} = \sqrt{\overline{l_u}^2 + \overline{m_u}^2}$	Characteristic wavenumber of the flow
	$\overline{k_B} = \sqrt{\overline{l_B}^2 + \overline{m_B}^2}$	Characteristic wavenumber of the **B** field
	$C_{\omega z} = \dfrac{\sum_{s,\phi}\left|\langle\boldsymbol{\omega}'\cdot\hat{\mathbf{z}}\rangle_z\right|}{\sum_{s,\phi}\langle|\boldsymbol{\omega}'|\rangle_z}$	Axial vorticity columnarity
	$H_z^{rel} = \dfrac{\langle H_z\rangle_h}{(\langle u_z u_z\rangle_h \langle\omega_z\omega_z\rangle_h)^{1/2}}$	Relative axial helicity
Nusselt number	$Nu = \dfrac{r_o}{r_i}\dfrac{qD}{\rho C_p \kappa \Delta T}$	Total heat transfer / Conductive heat transfer
Reynolds number	$Re = \dfrac{UD}{\nu} = \sqrt{2\mathcal{E}_K}$	Inertial force / Viscous force
Convective Reynolds number	$Re_c = \dfrac{U_c D}{\nu} = \sqrt{2\mathcal{E}_K^c}$	Convective inertial force / Viscous force
Magnetic Reynolds number	$Rm = \dfrac{UD}{\eta} = Re\,Pm$	Magnetic induction / Magnetic diffusion
Dipolarity	$f = \left(\dfrac{\int \mathbf{B}_{l=1}(r=r_o)\cdot\mathbf{B}_{l=1}(r=r_o)\,dA}{\int \mathbf{B}(r=r_o)\cdot\mathbf{B}(r=r_o)\,dA}\right)^{1/2}$	Dipole field strength (r_o) / Total field strength (r_o)
Imposed Elsasser number	$\Lambda_i = \dfrac{B^2}{2\rho\mu_o\eta\Omega} = \mathcal{E}_M Pm E$	Lorentz force / Coriolis force (low Rm)
Dynamic Elsasser number	$\Lambda_d = \dfrac{B^2}{2\rho\mu_o\Omega U\ell_B} = \dfrac{\Lambda_i}{Rm}\dfrac{D}{\ell_B}$	Lorentz force / Coriolis force (high Rm)
Lehnert number	$\lambda = \dfrac{B}{2\ell_B\Omega\sqrt{\rho\mu_o}} = A\Lambda_d$	Lorentz force / Coriolis force ($A = \mathcal{O}(1)$)
Alfvén number	$A = \dfrac{U\sqrt{\rho\mu_o}}{B} = \sqrt{\dfrac{Re^2 E Pm}{\Lambda_i}}$	Flow speed / Alfven wave speed

Christensen et al., 1999; Zhang and Schubert, 2000; Jones, 2007; Jault, 2008; Busse and Simitev, 2011). Further, King et al. (2010) have shown that heat transfer scaling laws from non-magnetic planar convection also apply to planetary dynamo models, regardless of magnetic field strength. These results imply that the traditional force balance argument from linear analysis using the Elsasser number Λ_i may not be an adequate measure of the dynamical influence of the Lorentz force in convection systems. Alternate characterizations of the Lorentz to Coriolis force ratio must therefore be considered.

Here, we contrast dynamo models with non-magnetic, but otherwise identical, rotating convection models to quantify the influence of magnetic fields on convective dynamics. While comparisons between dynamo and non-magnetic simulations have been conducted (e.g., Christensen et al., 1999; Grote and Busse, 2001; Aubert, 2005), these studies are typically limited to convection less than 40 times critical and dipolar magnetic field geometries. Our survey is complementary to these earlier studies as it extends the comparison to convection more than 1000 times critical, considers both dipolar and multipolar magnetic fields, and makes no assumptions of azimuthal symmetries.

We measure the strengths and structures of magnetic fields and fluid motions, as well as heat transfer efficiency. We focus on, in order of priority, (i) the effect of the presence of magnetic fields on convection, (ii) the effect of varying convective vigor, and (iii) the effect of varying the rotation rate. In Section 2, we detail the model and methods. Behavioral regimes found in our models with fixed $E = 10^{-4}$ are discussed in Section 3, and we analyze parametrizations of the magnetic field influence in Section 4. In Section 5, we examine the transition from dipolar to multipolar dynamos. Section 6 investigates the influence of varying the Ekman number, while Section 7 applies our results to planetary cores. Our conclusions are given in Section 8.

2. Numerical model

We use the numerical model MagIC 3.38 (Wicht, 2002; Christensen and Wicht, 2007), which is based on the original pseudospectral code of Glatzmaier (1984). This model simulates three-dimensional, time-dependent thermal convection of a Boussinesq fluid in a spherical shell rotating with constant angular velocity $\Omega \hat{\mathbf{z}}$. We conduct two sets of simulations: (i) non-magnetic rotating convection models which employ an electrically insulating fluid and (ii) dynamo models which employ an electrically conducting fluid. The shell geometry is defined by the ratio of the inner to outer shell radii, $\chi = r_i/r_o = 0.4$. The shell boundaries are isothermal with an imposed (superadiabatic) temperature contrast ΔT between the inner and outer boundaries. The mechanical boundary conditions are impenetrable and no-slip. Gravity varies linearly with spherical radius. The region exterior to the fluid shell is electrically insulating, and the electrical conductivity of the rigid inner sphere is chosen to be the same as that of the convecting fluid region.

The dimensionless governing equations for this system are

$$E\left(\frac{\partial \mathbf{u}}{\partial t} + \mathbf{u} \cdot \nabla \mathbf{u} - \nabla^2 \mathbf{u}\right) + \hat{\mathbf{z}} \times \mathbf{u} + \frac{1}{2}\nabla p = \frac{RaE}{Pr}\frac{\mathbf{r}}{r_o}T + \frac{1}{2Pm}(\nabla \times \mathbf{B}) \times \mathbf{B},$$
(1)

$$\frac{\partial \mathbf{B}}{\partial t} = \nabla \times (\mathbf{u} \times \mathbf{B}) + \frac{1}{Pm}\nabla^2 \mathbf{B},$$
(2)

$$\frac{\partial T}{\partial t} + \mathbf{u} \cdot \nabla T = \frac{1}{Pr}\nabla^2 T,$$
(3)

$$\nabla \cdot \mathbf{u} = 0, \quad \nabla \cdot \mathbf{B} = 0,$$
(4)

where $\mathbf{u}$ is the velocity vector, $\mathbf{B}$ is the magnetic induction, T is the temperature, and p is the non-hydrostatic pressure. We make use of typical non-dimensionalizations used in the planetary dynamo literature: shell thickness $D = r_o - r_i$ as length scale; ΔT as temperature scale; $\tau_v \sim D^2/v$ as time scale; $\rho v \Omega$ as pressure scale; v/D as velocity scale such that the non-dimensional globally averaged rms flow velocity is equal to the Reynolds number $Re = UD/v$; and $\sqrt{2\rho\mu_o\eta\Omega}$ as magnetic induction scale such that the square of the non-dimensional globally averaged rms magnetic field strength is equal to the traditionally defined Elsasser number $\Lambda_i = B^2/2\rho\mu_o\eta\Omega$. In these definitions, ρ is the density, v is the kinematic viscosity, κ is the thermal diffusivity, η is the magnetic diffusivity, μ_o is the magnetic permeability of free space, and α is the thermal expansion coefficient.

The non-dimensional control parameters are the shell geometry $\chi = r_i/r_o$, the Rayleigh number $Ra = \alpha g_o \Delta T D^3/v\kappa$, the Ekman number $E = v/2\Omega D^2$, the Prandtl number $Pr = v/\kappa$, and the magnetic Prandtl number $Pm = v/\eta$. The Rayleigh number characterizes the ratio of buoyancy to diffusion. The Ekman number characterizes the ratio of viscous to Coriolis forces. The Prandtl numbers Pr and Pm characterize the ratio of viscous to thermal and magnetic diffusivities, respectively. The control parameter definitions are summarized in Table 1; the diagnostic parameters are defined in Table 2.

Our suite of simulations consists of 36 planetary dynamo models and 30 non-magnetic rotating convection models. This survey considers Prandtl number $Pr = 1$, magnetic Prandtl numbers up to $Pm = 5$, Ekman numbers in the range $10^{-3} \geq E \geq 10^{-5}$, and Rayleigh numbers from near onset to more than 1000 times critical. The critical Rayleigh number, Ra_c, denotes the onset of convection. Here, we use the inferred scaling $Ra_c = 3.5E^{-4/3}$ from King et al. (2010). The Rayleigh numbers then fall in the range $1.9Ra_c \leq Ra \leq 1125Ra_c$. This dataset, given in Supplementary Tables 4 and 5, is among the broadest surveys of supercriticality made to date.

The value of Pm is chosen such that the magnetic Reynolds number $Rm = Re\,Pm \gtrsim 10^2$, a necessary condition for dynamo action. For most of our simulations, the parameters are fixed to the following values, which are commonly used in the current planetary dynamo literature: $E = 10^{-4}$, $Pr = 1$, and $Pm = [0, 2]$. Dynamo models with similar parameters values have been argued to generate Earth-like magnetic field morphologies (Christensen et al., 2010; Christensen, 2011).

The largest numerical grid uses 213 spherical harmonic modes, 65 radial levels in the outer shell, and 17 radial levels in the inner core. No azimuthal symmetries are employed. Dynamo models are initialized using the results of prior dynamo simulations. Non-magnetic models are initialized by turning off the magnetic field of the associated dynamo model, similar to Zhang et al. (1998) among others. Some studies have found initial conditions to be important (e.g., Simitev and Busse, 2009; Sreenivasan and Jones, 2011; Dormy, 2011), owing to bistable dynamo states. Thus, we test for bistability by comparing results obtained with different initial conditions for a limited number of cases and find no significant differences in time-averaged behaviors. Once the initial transient behavior has subsided, time-averaged properties for cases with $Ra \leq 11Ra_c$ are averaged over at least $\tau_\Omega \sim \tau_v/\pi E > 1500$ rotations, cases with $11Ra_c < Ra \leq 56Ra_c$ are averaged over at least 500 rotations, and all other cases are averaged over at least 30 rotations.

Hyperdiffusion is used in five of our 66 simulations. It is applied in our most supercritical models ($Ra \geq 562Ra_c$ for $E = 10^{-4}$; $Ra = 12.5Ra_c$ for $E = 10^{-5}$) to increase numerical stability by damping the small-scale components of the velocity, thermal, and magnetic fields. In these models, the viscous, thermal, and magnetic

Table 3
Summary of the hyperdiffusion parameters used in this study. Parameter definitions are given in (5).

Ra	Ra/Ra_c	E	Pm	l_{max}	A_{HD}	l_{HD}	β
2.10×10^7	28	10^{-4}	2	128	10	20	2
4.24×10^8	562	10^{-4}	2	192	5	50	2
4.24×10^8	562	10^{-4}	0	192	5	50	2
8.48×10^8	1125	10^{-4}	2	192	10	20	2
2.00×10^8	12.5	10^{-5}	2	213	0.05	150	2

diffusivities are multiplied by a factor

$$d(l) = 1 + A_{HD}\left(\frac{l+1-l_{HD}}{l_{max}+1-l_{HD}}\right)^{\beta}, \qquad (5)$$

where A_{HD} is the hyperdiffusion amplitude, l is the spherical harmonic degree, l_{HD} is the degree above which hyperdiffusion starts to act, l_{max} is the maximum harmonic degree, and β is the exponent of hyperdiffusion. As shown in Table 3, the strongest form of hyperdiffusion used in this study has $A_{HD} = 10$, $l_{HD} = 20$, $\beta = 2$, and $l_{max} = 192$. The harmonic degree above which hyperdiffusion applies, l_{HD}, was chosen to be greater than the characteristic harmonic degree of the flows, $\overline{l_u}$. By comparing a hyperdiffusive dynamo model at $Ra = 28Ra_c$ and $E = 10^{-4}$ to an otherwise identical non-hyperdiffusive model, we have determined that this hyperdiffusion does not significantly affect the flow speeds or heat transfer. The Reynolds and Nusselt numbers differ by less than 3%. However, the characteristic harmonic wavenumber of the flow decreases by 16% in the hyperdiffusive model, and the traditional Elsasser number and dipolarity both increase by about 35%. Thus, the use of hyperdiffusion generally leads to broader scale flows (Zhang and Schubert, 2000) and strengthens the dipole component of the magnetic field. We further note that none of the five models that use hyperdiffusion are near the dipolarity or columnarity transitions discussed below.

3. Results of the $E = 10^{-4}$ survey

We focus first on the role of magnetic fields in our models with $E = 10^{-4}$. As the Rayleigh number is varied, we observe three behavioral regimes based on magnetic field morphology and convective planform. Models in Regime I ($Ra \lesssim 5.0Ra_c$) are characterized by columnar convection and dipole-dominated magnetic fields, while models in Regime II ($5.1Ra_c \lesssim Ra \lesssim 19Ra_c$) have columnar convection and multipolar magnetic fields. In Regime III ($Ra \gtrsim 19Ra_c$), models are characterized by three-dimensional convection and multipolar magnetic fields. In this section, we discuss the characteristics of model-generated flows and fields in the context of these three regimes.

3.1. Magnetic field morphology

The basic magnetic field morphology is quantified by its dipolarity

$$f = \left(\frac{\int \mathbf{B}_{l=1}(r=r_o) \cdot \mathbf{B}_{l=1}(r=r_o)dA}{\int \mathbf{B}(r=r_o) \cdot \mathbf{B}(r=r_o)\,dA}\right)^{1/2}, \qquad (6)$$

here $\mathbf{B}(r=r_o)$ is the magnetic induction vector at the outer shell boundary, $l=1$ indicates the dipolar component, and $\int dA$ integrates over the outer spherical shell surface. The magnetic field is perfectly dipolar when $f=1$. We consider cases with $f \gtrsim 0.5$ to be dipole-dominated. The dipolarity of Earth's magnetic field at the core–mantle boundary up to spherical harmonic degree 12 is $f \approx 0.68$. Previous dynamo studies characterize magnetic field dipolarity using surface fields up to harmonic degree $l=12$ (Christensen and Aubert, 2006) and $l=8$ (Christensen et al.,

2010). Here, we calculate f using the full spectrum in order to best characterize the model-generated fields. The $f(Ra)$ behavior is similar when the calculation of dipolarity is truncated at $l=12$.

Fig. 1 shows the time-averaged dipolarity plotted versus the Rayleigh number for the $E = 10^{-4}$ models. A first order transition between dipole-dominated ($f \gtrsim 0.55$) and multipolar ($f \lesssim 0.21$) magnetic fields occurs at $Ra = 5.1Ra_c$. This defines the boundary between Regimes I and II. The boundary between Regimes II and III (dashed vertical line) is defined based on columnarity, discussed in Section 3.2.

Fig. 2 (top row) shows the radial magnetic field intensity near the outer shell boundary for four dynamo models with $Ra = 1.9Ra_c$, $4.9Ra_c$, $5.6Ra_c$, and $562Ra_c$. These visualizations illustrate how the magnetic field structure changes across the three regimes.

3.2. Characteristics of convection

Convection is characterized visually, as well as quantitatively via measurements of length scales, columnarity, helicity, flow speeds, and heat transfer.

#### 3.2.1. Flow visualizations

Fig. 2 also shows snapshots of axial vorticity $\omega_z = \hat{\mathbf{z}} \cdot (\nabla \times \mathbf{u})$ isosurfaces for select dynamo and non-magnetic models. These flow visualizations illustrate that the axial alignment of convective structures outside of the tangent cylinder persists from near onset to $Ra \approx 19Ra_c$, regardless of the presence of strong magnetic fields. (The tangent cylinder is the imaginary right cylinder that circumscribes the inner shell's equator.) Above $Ra \approx 19Ra_c$, the columnar nature of the flow is destroyed in both dynamo and non-magnetic models. This transition in flow field morphology defines the boundary between Regimes II and III. In Regime III, convection becomes strongly three-dimensional.

3.2.2. Length scales

Linear theory predicts a fundamental change in characteristic length scale between $m = \mathcal{O}(E^{-1/3}D)$ as $E \to 0$ in non-magnetic systems and $m = \mathcal{O}(D)$ when a strong magnetic field with
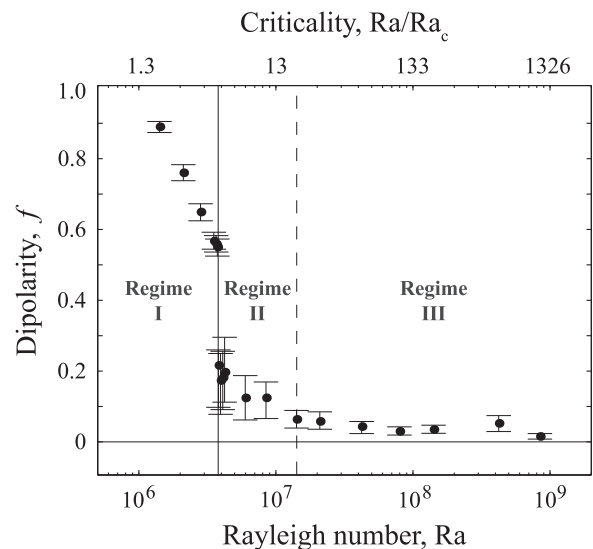
Fig. 1. Time-averaged dipolarity, f, versus the Rayleigh number for the $E = 10^{-4}$ models. Error bars represent ± 1 standard deviation of dipolarity over time. The solid vertical line at $Ra = 3.82 \times 10^6$ indicates the sharp transition between dipolar and multipolar dynamos, and the long-dashed vertical line at $Ra = 1.42 \times 10^7$ indicates where the convective flow structures are no longer dominantly axial, based on the columnarity calculations shown in Fig. 3a.
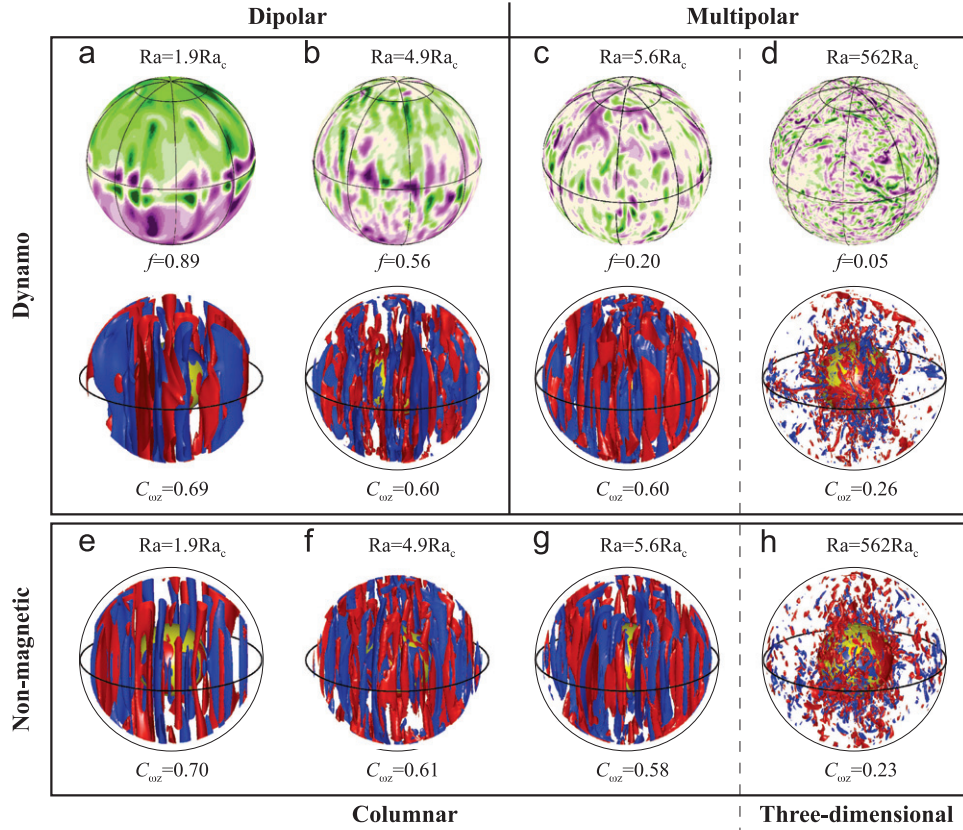
Fig. 2. Instantaneous radial magnetic fields near the outer shell boundary (top row) and isosurfaces of instantaneous axial vorticity for select $E = 10^{-4}$ dynamo (middle row) and non-magnetic (bottom row) models. Purple (green) indicates radially outward (inward) directed magnetic fields. Red (blue) indicates cyclonic (anticyclonic) vorticity. Each subplot has its own color scale. The inner yellow sphere represents the inner shell boundary. The outer boundary layer has been excluded for clarity. Below each image is either the dipolarity, f, or the axial vorticity columnarity, C_{ω_z}. (For interpretation of the references to color in this figure caption, the reader is referred to the web version of this article.)

$\Lambda_i \gtrsim \mathcal{O}(1)$ is imposed in the limit $E \rightarrow 0$ (Chandrasekhar, 1961). This prediction is tested by comparing the characteristic wavenumbers of the flow field in the dynamo and non-magnetic models

$$\overline{k_u} = \sqrt{\overline{l_u}^2 + \overline{m_u}^2}, \tag{7a}$$

where

$$\overline{l_u} = \sum_{l=0}^{l=l_{max}} \frac{l(\mathbf{u}_l \cdot \mathbf{u}_l)}{2\mathcal{E}_K} \tag{7b}$$

and

$$\overline{m_u} = \sum_{m=0}^{m=m_{max}} \frac{m(\mathbf{u}_m \cdot \mathbf{u}_m)}{2\mathcal{E}_K}, \tag{7c}$$

here $\mathbf{u}_l$ is the velocity at spherical harmonic degree l, $\mathbf{u}_m$ is the velocity at spherical harmonic order m, and $\mathcal{E}_K$ is the kinetic energy. The time-averaged values, given in Supplementary Table 6, show that the presence of dynamo-generated magnetic fields alters the value of $\overline{k_u}$ by at most 14% in comparison to the associated non-magnetic cases. Thus, these dynamo models do not produce the fundamental change in length scale that linear theory predicts.

3.2.3. Columnarity

We can also quantify the style of convection using axial vorticity measurements. Quasigeostrophic convection is dominated by axial, vortical columns that extend in $\hat{\mathbf{z}}$ across the entire shell. We define 'columnarity' using a measure of the axial variations of axial vorticity, ω_z, in the bulk fluid outside of the tangent cylinder

$$C_{\omega z} = \frac{\sum_{s,\phi} |\langle \boldsymbol{\omega}' \cdot \hat{\mathbf{z}} \rangle_z|}{\sum_{s,\phi} \langle |\boldsymbol{\omega}'| \rangle_z}, \tag{8}$$

here $\langle \rangle_z$ indicates averages in the axial $\hat{\mathbf{z}}$ direction, $\boldsymbol{\omega}'$ indicates vorticity calculated using only the non-axisymmetric velocity field, and the summation occurs over the equatorial plane (s, ϕ). Columnar convection has relatively large columnarity, $C_{\omega z} \gtrsim 0.5$, because vorticity, $\boldsymbol{\omega}'$, is dominated by its axial component, $\boldsymbol{\omega}' \cdot \hat{\mathbf{z}}$. We consider cases with $C_{\omega z} \gtrsim 0.5$ to be columnar, similar to our convention for f. Thus, we define the transition between Regimes II and III to occur where $C \approx 0.5$. Comparison of axial vorticity isosurfaces shows this convention to be an adequate proxy for the breakdown of columnar convection.

Fig. 3a shows columnarity as a function of the Rayleigh number for the $E = 10^{-4}$ models. The $C_{\omega z}$ values agree to within an average of 4% between the dynamo and non-magnetic models, with a maximum difference of 14%. The presence of magnetic fields, therefore, does not change the basic planform of convection.

Columnar convection breaks down near $Ra = 19Ra_c$, where $C_{\omega z} < 0.5$ (Fig. 3a). King et al. (2009, 2010) argue that the breakdown of columnar convection occurs when the thermal boundary layer becomes thinner than the Ekman boundary layer. We calculate these boundary layer thicknesses and find that they indeed cross at the transition between Regimes II and III.

This columnarity transition does not, however, coincide with the magnetic field morphology transition at $Ra = 5.1Ra_c$. Therefore, columnar convection can generate both dipolar (Regime I) and multipolar (Regime II) magnetic fields. It is also worth noting
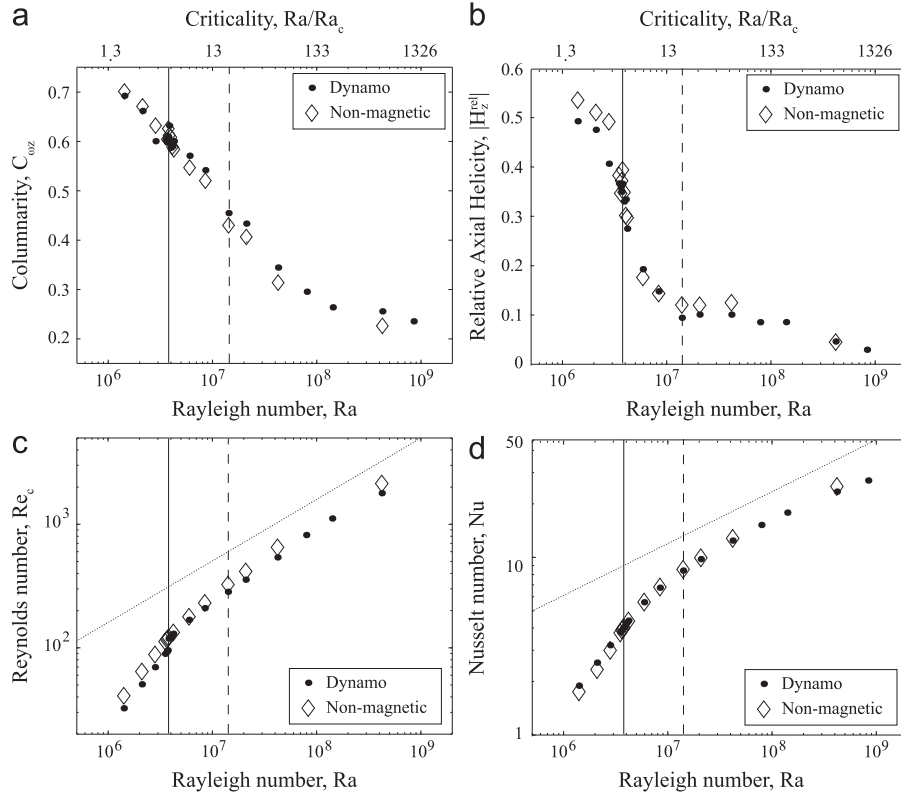
Fig. 3. (a) Instantaneous axial vorticity columnarity, $C_{\omega z}$, (b) instantaneous relative axial helicity, $|H_z^{rel}|$, (c) time-averaged convective flow speeds, Re_c, and (d) time-averaged heat transfer efficiency, Nu, as a function of the Rayleigh number for the $E = 10^{-4}$ models. The dotted lines indicate classic scalings for non-rotating, non-magnetic convection: (c) $Re_c \propto Ra^{1/2}$ and (d) $Nu \propto Ra^{2/7}$. In each plot, the solid and long-dashed vertical lines indicate transitions in dipolarity and columnarity, respectively, defined in the Fig. 1 caption.

that, in contrast to the sharp transition in dipolarity, $C_{\omega z}$ tends to decrease gradually with increased Rayleigh number such that a first order transition does not occur.

3.2.4. Helicity

Helicity is common to rotating convection systems and is thought to be essential to large-scale magnetic field generation (e.g., Parker, 1955; Moffatt, 1978; Roberts, 2007). Helical flow is the corkscrew-like motion produced by correlations between velocity and vorticity fields. Here, we consider axial helicity, $H_z = u_z \omega_z$. Relative axial helicity is defined as axial helicity normalized by its maximum possible value

$$H_z^{rel} = \frac{\langle H_z \rangle_h}{(\langle u_z u_z \rangle_h \langle \omega_z \omega_z \rangle_h)^{1/2}}, \qquad (9)$$

where $\langle \rangle_h$ is the volumetric average in each hemisphere excluding boundary layers (e.g., Olson et al., 1999; Schmitz and Tilgner, 2010, cf. Sreenivasan and Jones, 2011). Since axial helicity tends to be anti-symmetric across the equator, we report the average helicity magnitude averaged over both hemispheres, $|H_z^{rel}|$.

Fig. 3b shows calculations of relative axial helicity plotted versus the Rayleigh number. Helicity is not appreciably sensitive to the presence of magnetic fields in these models; our dynamo and non-magnetic simulations produce $|H_z^{rel}|$ values that typically differ by less than 10%. Helicity is diminished by increased thermal forcing (Ra). Regime I models exhibit strongly helical flows with $|H_z^{rel}| \gtrsim 0.4$. Near the Regimes I and II boundary ($3.8 \leq Ra/Ra_c \leq 8.0$), helicity drops off significantly. The three-dimensional flows in Regime III models are poorly correlated, such that $|H_z^{rel}| \lesssim 0.1$.

The degradation of helical flow occurs at lower Rayleigh numbers than where columnar convection breaks down. This

implies that changes in axial vorticity are not responsible for the helicity decrease. The breakdown of helicity is, however, coincident with the dipolarity transition in Fig. 1. We discuss this in further detail in Section 5.

3.2.5. Convective flow speeds

Convective flow speeds are given by the convective Reynolds number $Re_c = U_c D/\nu$, where U_c is the rms flow speed excluding the axisymmetric zonal flow component. Zonal flows are weak in our models due to the no-slip boundaries; non-zonal flow speeds, Re_c, and total flow speeds, Re, differ by than less than 13% in all of our $E = 10^{-4}$ models. This difference is maximum for the strongly supercritical models where relatively strong zonal flows can develop.

Fig. 3c plots the time-averaged convective Reynolds number versus the Rayleigh number. The non-magnetic models have Re_c values that are on average 13% stronger than those of associated dynamos, with a maximum difference of 21%. This indicates that flow speeds are reduced by the Lorentz force as kinetic energy is transferred to magnetic energy. Fig. 3c shows that the convective flow speeds, however, are more sensitive to thermal driving (Ra) than the presence of magnetic fields.

The dotted line in Fig. 3c shows the classic $Re \propto Ra^{1/2}$ 'free-fall' scaling law found in non-magnetic, non-rotating turbulent convection (e.g., Sano et al., 1989; Castaing et al., 1989; Siggia, 1994; Tilgner, 1996). Our data roughly follow this scaling in Regime III, which suggests that neither magnetic fields nor rotation strongly influence these cases.

3.2.6. Heat transfer

Fig. 3d shows the time-averaged heat transfer behavior plotted versus the Rayleigh number. The Nusselt number, Nu, is the ratio

of total to conductive heat transfer

$$Nu = \frac{r_o}{r_i} \frac{qD}{\rho C_p \kappa \Delta T}, \tag{10}$$

where q is the heat flux per unit area on the outer shell boundary and C_p is the specific heat capacity. Between the dynamo and non-magnetic models, the Nusselt numbers agree to within an average of 3%, with a maximum difference of 10%. In Regime I, the presence of magnetic fields tends to produce slightly larger radial length scales (see Supplementary Table 4) that transport heat more efficiently. In Regime III, magnetic fields weakly damp flow speeds (Fig. 3c), tending to reduce heat transport. Overall, the magnetic field has a second order influence on heat transport in these models. The classic $Nu \propto Ra^{2/7}$ scaling law often found in non-magnetic, non-rotating turbulent convection systems (e.g., Castaing et al., 1989; Glazier et al., 1999) is superimposed in Fig. 3d. A comparison of our data against this scaling further supports our contention that inertially dominated convection occurs in Regime III.

3.3. Force integrals

The competition between Lorentz (F_L), Coriolis (F_C), inertial (F_I), and viscous (F_V) forces can be quantified by comparing terms in the momentum equation. Toward this end, the forces are integrated over the entire spherical shell volume: $F = \int_V (\mathcal{F}_r^2 + \mathcal{F}_\theta^2 + \mathcal{F}_\phi^2)^{1/2} \, dV$ where $\mathcal{F}$ is a generic force density. Boundary layers are included in the integration, but their exclusion does not significantly affect the results, with the exception of the viscous force integral where up to 50% of the force is contained within the boundary layer.

Fig. 4 shows these force integral calculations and their ratios for all dynamo and non-magnetic models with $E = 10^{-4}$. In both sets of models, the Coriolis term dominates in Regimes I and II, indicating that these models are in quasigeostrophic balance,

consistent with the prevalence of columnar convection within these regimes.

The Lorentz force is not a dominant influence on convection dynamics in these models. The ratio of Lorentz to Coriolis forces does not exceed 0.3 in Regimes I and II, while the ratio of Lorentz to inertial forces is less than 0.7 in Regimes II and III. This subdominance of the Lorentz force explains why our dynamo and rotating convection models exhibit similar behaviors. In similar models, it has been found that the Lorentz force is spatially intermittent (e.g., Sreenivasan and Jones, 2006; Aubert et al., 2008). So although the Lorentz force is globally subdominant, it can be dynamically important in the sparse regions of strong magnetic field intensification.

3.4. Zonal flows

While we are primarily focused on the convective, non-zonal dynamics in this paper, we also note that a first order change in the style of zonal flow occurs between dipolar and multipolar dynamo models. Aubert (2005) shows that dipolar magnetic fields play a critical role in the zonal flow power budget, yet we find that the non-zonal convection tends not to be strongly sensitive to magnetic fields in our $E = 10^{-4}$ models. This difference in behavior occurs because the pressure gradient term can balance the Coriolis force in the full momentum equation, but is identically zero in the axisymmetric azimuthal momentum equation. As a result, the convective flows are quasigeostrophic, while the geostrophic force balance cannot be established for the zonal flow (e.g., Roberts and Aurnou, 2011). The Lorentz force must then balance the Coriolis force in the zonal momentum equation when the inertial and viscous forces are weak. Consequently, this leads to first order differences in zonal flows between the dynamo and associated non-magnetic models.
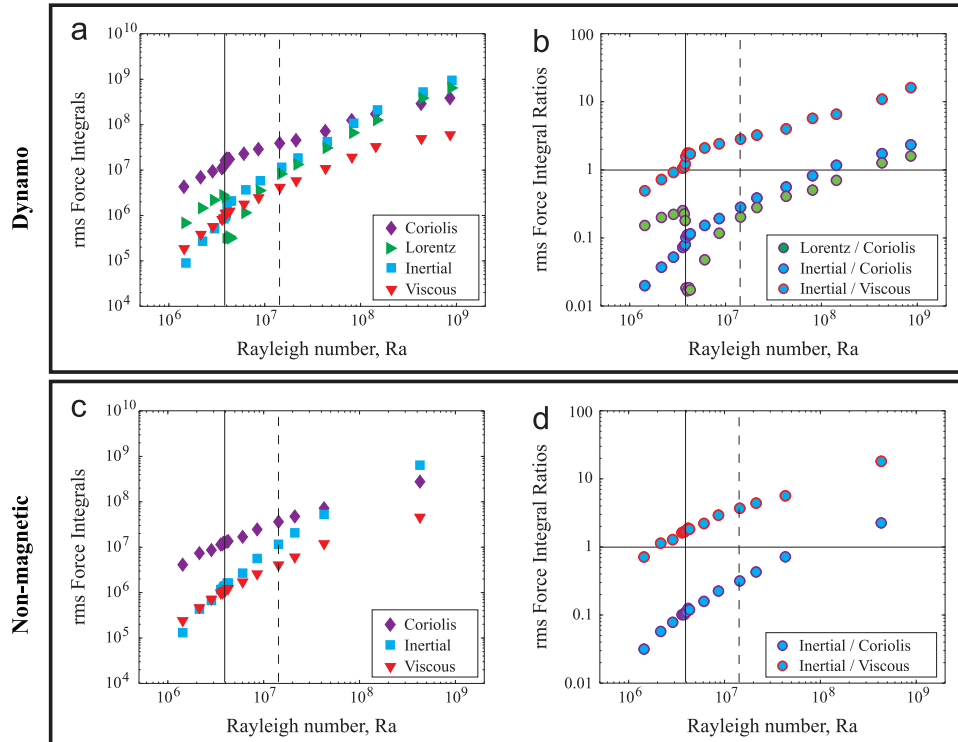
Fig. 4. (a) and (c), respectively, plot instantaneous integrals of the rms Coriolis, Lorentz, inertial, and viscous forces versus the Rayleigh number for the $E = 10^{-4}$ dynamo and non-magnetic models. Ratios of the force integrals are shown in (b) and (d) for the dynamo and non-magnetic models, respectively. In each plot, the solid and long-dashed vertical lines indicate transitions in dipolarity and columnarity, respectively, defined in the Fig. 1 caption.

4. Parametrization of magnetic field influence

In this section, we compare calculations and parametrizations of the Lorentz to Coriolis force ratios in our $E = 10^{-4}$ models.

4.1. Traditional Elsasser number

Following the developments of Christensen et al. (1999) and Cardin et al. (2002), the ratio of the Lorentz force ($\mathbf{J} \times \mathbf{B}/\rho$) to Coriolis force ($2\mathbf{\Omega} \times \mathbf{u}$) is parametrized by the general form of the Elsasser number

$$\Lambda = \frac{JB}{2\rho\Omega U}. \tag{11}$$

In order to estimate Λ using rms magnetic field strength B, the current density J is characterized via either Ohm's law

$$\mathbf{J} = \sigma(\mathbf{E} + \mathbf{u} \times \mathbf{B}) \tag{12}$$

(where $\sigma = 1/\mu_o\eta$ is the electrical conductivity), or Ampere's law under the MHD approximation

$$\mathbf{J} = \frac{1}{\mu_o}\nabla \times \mathbf{B}. \tag{13}$$

Using (12) in (11), the contribution to current density from the electrical field E is typically discarded, giving $J \sim \sigma UB$ and yielding the traditional form of the Elsasser number

$$\Lambda_i = \frac{B^2}{2\rho\mu_o\eta\Omega}. \tag{14}$$

The benefit of this parameterization is that its components can be determined by relatively straightforward observations of planetary bodies.

Fig. 5 compares Λ_i against the ratio of the Lorentz and Coriolis force integrals from Fig. 4b. The explicitly calculated force integral ratios range over $0.02 \leq F_L/F_C \leq 1.6$, with a mean of 0.3. This demonstrates that the volume-averaged Lorentz force is dynamically weak with respect to the Coriolis force in most of our models with $E = 10^{-4}$. In contrast, the traditional Elsasser numbers are typically greater than unity, with a mean value of 20 and a range between $0.2 \leq \Lambda_i \leq 200$. These relatively large values of Λ_i incorrectly imply that Lorentz forces should dominate. The traditional form of the Elsasser number then overestimates the strength of the Lorentz force, typically by a factor of approximately 10 in these dynamo models.
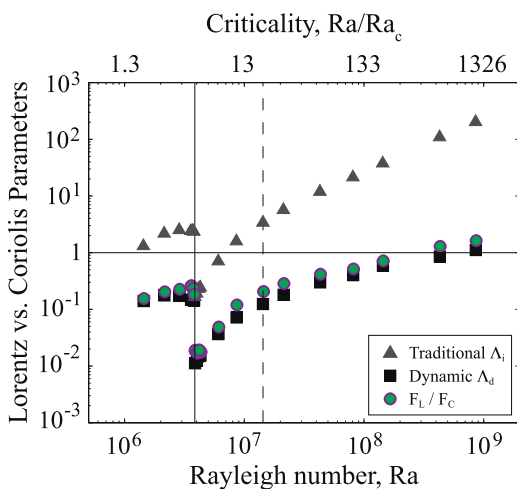
The misfit between Λ_i and the actual force ratio can be understood in terms of the two main assumptions that are made to arrive at $\Lambda = \Lambda_i$. First, this formulation assumes that $|\mathbf{u} \times \mathbf{B}| = UB$, which is not necessarily appropriate in a non-linear system in which the flow and field can self-organize such that interaction is more limited: $|\mathbf{u} \times \mathbf{B}| < UB$ (e.g., Zhang, 1995). Second, the assumption that $\mathbf{E} = 0$ physically implies that the magnetic field is not strongly time-variant. This can be seen by combining (12) and (13) to obtain the uncurled magnetic induction equation

$$\sigma\mathbf{E} + \sigma\mathbf{u} \times \mathbf{B} - \frac{1}{\mu_o}\nabla \times \mathbf{B} = 0. \tag{15}$$

The terms from left to right represent the time evolution, induction, and diffusion of magnetic field, respectively. By ignoring the contribution to current density from the electric field in (12) to get Λ_i, temporal variations of the magnetic field are neglected. This assumption is likely valid for MHD systems with *imposed* magnetic fields that do not vary strongly with time ($Rm < 1$), which motivates our use of the subscript 'i' for the traditional Elsasser number. However, most natural and simulated dynamos exhibit significant time variability ($Re > 1, Rm > 1$). Therefore, the traditional Elsasser number, Λ_i, may not accurately gauge the strength of the Lorentz force in dynamos.

4.2. Dynamic Elsasser number

The strength of the Lorentz force can be estimated without making these assumptions by using the form of current density from Ampere's law (13), so the current density can be parametrized as $J \sim B/\mu_o\ell_B$. We characterize magnetic field gradients using a typical quarter-wavelength of magnetic field variations: $\ell_B \sim (\pi D/2)/\overline{k_B}$, where

$$\overline{k_B} = \sqrt{\overline{l_B}^2 + \overline{m_B}^2} \tag{16}$$

analogous to $\overline{k_u}$ (see Table 2). This parametrization leads to the dynamic Elsasser number, Λ_d, in which the relative strength of Lorentz and Coriolis forces is estimated by

$$\Lambda_d = \frac{B^2}{2\rho\mu_o\Omega U\ell_B} = \frac{\Lambda_i}{Rm}\frac{D}{\ell_B}. \tag{17}$$

Fig. 5 shows calculations of Λ_d from our $E = 10^{-4}$ dynamo models. The values range over $0.01 \leq \Lambda_d \leq 1.1$ with a mean of 0.2, correctly predicting that the influence of magnetic fields on convection is secondary with respect to the Coriolis force in most of our models. Further, the dynamic Elsasser number is in good agreement with the Lorentz to Coriolis force integral ratios; the values differ by at most a factor of two.

Christensen et al. (1999) also calculate this parameter for a survey of dynamo models and find that the values typically range between 0.1 and 0.5 for $E \geq 10^{-4}$. However, they interpret their models to be in the 'strong-field' regime. This interpretation contrasts with our observation that magnetic fields have a second order influence on convection at these Ekman numbers.

4.3. Lehnert number

Another parameter used to characterize the competing roles of Lorentz and Coriolis forces is the Lehnert number, λ (Lehnert, 1954; Fearn et al., 1988). This parameter has been employed by recent studies that consider the effects of imposed magnetic fields on transient motions in rapidly rotating spherical shells (Jault, 2008; Gillet et al., 2011). The Lehnert number quantifies this force ratio by comparing the angular rotation frequency to an Alfvén wave frequency. As such, λ can be interpreted as a special case of

Fig. 5. Comparison of the calculated Lorentz to Coriolis force integral ratios, F_L/F_C, against the traditional and dynamic Elsasser numbers as a function of the Rayleigh number for the $E = 10^{-4}$ models. The solid and long-dashed vertical lines indicate transitions in dipolarity and columnarity, respectively, defined in the Fig. 1 caption.

the dynamic Elsasser number, Λ_d, where the typical flow speed U is assumed to scale as an Alfvén wave speed, $V_A = B/\sqrt{\rho\mu_o}$. Substituting $U = V_A$ into (17) produces the Lehnert number

$$\lambda = \frac{B}{2\ell_B\Omega\sqrt{\rho\mu_o}} = A\Lambda_d, \tag{18}$$

where the Alfvén number, $A = U/V_A$, is the ratio of the flow velocity to the Alfvén wave speed. Thus, when flow speeds follow the Alfvén wave speed scaling, $A = \mathcal{O}(1)$, the Lehnert number should aptly characterize this force balance. For example, in studies of transient flow with strong, imposed fields (Jault, 2008) or analysis of torsional Alfvén wave propagation in Earth's core (Gillet et al., 2011), λ is the relevant parameter. However, in many planetary dynamo models, the typical flow speeds and magnetic field strengths are not found to be related by $A \approx 1$ (cf. Christensen and Aubert, 2006). Therefore, we argue that Λ_d provides a more general estimation of the Lorentz to Coriolis force ratio for dynamos.

5. Breakdown of dipolar magnetic field generation

We observe a sharp transition from dipolar to multipolar magnetic fields at the boundary between Regimes I and II in our $E = 10^{-4}$ models (Fig. 1). Poloidal magnetic fields, including the dipole component, are generated by the α-effect in planetary dynamo models (Christensen and Wicht, 2007). The α-effect describes the generation of large-scale fields by strongly correlated flows, which, for planetary and stellar dynamos, is typically attributed to the helical nature of rotating convection (e.g., Parker, 1955; Jones, 2011).

Comparing Figs. 1 and 3b, we observe that both dipole-dominance and helical flow break down near the Regimes I and II boundary. Since helical flow is a necessary ingredient for large-scale dynamo generation (e.g., Parker, 1955), the degradation of relative helicity (Fig. 3b) likely causes the collapse of the dipole field (Fig. 1). Importantly, the change in helicity across this regime boundary occurs *even in the absence of magnetic fields*, implying that the breakdown in helicity is a hydrodynamic process. This suggests that the Lorentz force does not strongly influence the transition from dipolar to multipolar field generation, which is instead a predominantly hydrodynamic transition. The mechanism responsible for this hydrodynamic helicity transition, however, is not currently well understood.

Several studies have suggested that the breakdown of dipolar field generation is the result of a competition between inertial and Coriolis forces (e.g., Sreenivasan and Jones, 2006; Christensen and Aubert, 2006; Olson and Christensen, 2006; Christensen, 2010). We observe in Fig. 4b, however, that the calculated Coriolis force is an order of magnitude stronger than inertia where this field morphology transition occurs. The dominance of the Coriolis force in both regimes suggests that the transition in helical flow and field morphology is caused instead by competition between second order hydrodynamic forces. Specifically, near the Regimes I and II boundary, we find that inertia becomes stronger than viscosity. We then hypothesize that the role of viscosity is important for helical flow and, therefore, for the generation of dipolar fields in these models with $E = 10^{-4}$.

6. Influence of varying Ekman number

Our simulations carried out at $E = 10^{-4}$ demonstrate that the magnetic field does not play a dominant role in convection dynamics, including axial vorticity columnarity, relative axial helicity, flow speeds, and heat transfer efficiency. Of these

characteristics, helicity is of particular importance since it is found to be necessary for the generation of dipolar magnetic fields. Our models also show that the Lorentz to Coriolis force ratio is well-described by the dynamic Elsasser number. Here, we test the applicability of these results to simulations with different Ekman numbers ($10^{-3} \geq E \geq 10^{-5}$).

Fig. 6a shows time-averaged dipolarity plotted versus the Rayleigh number for all of our models. A first order transition between dipole-dominated ($f \gtrsim 0.5$) and multipolar ($f \lesssim 0.3$) magnetic fields occurs in the $E \geq 10^{-4}$ models. This transition appears to be more gradual in the $E = 10^{-5}$ models where $f \gtrsim 0.3$ and no pronounced dichotomy between dipolar and multipolar dynamos is found.

Fig. 6b shows that relative helicity is diminished by increasing the Rayleigh number and by decreasing the Ekman number. Thus, our most helical models are found to lie near the onset of convection (low Ra) and to occur for the largest Ekman number, where we expect the role of viscosity to be strongest. The influence of magnetic fields on helicity also changes with the Ekman number. While magnetic fields typically modify the relative helicity values by less than 20% in the $E \geq 10^{-4}$ models, relative helicity is decreased by up to 80% by the presence of magnetic fields in the $E = 10^{-5}$ models. Thus, magnetic fields produce first order changes in relative helicity in our lowest Ekman number simulations.

A comparison between dipolarity and relative axial helicity (panels a and b of Fig. 6) shows that the breakdown of the magnetic dipole coincides with the degradation of helical flow for all Ekman numbers considered. As the role of viscosity is reduced ($E < 10^{-4}$), the transition in magnetic field morphology becomes more gradual. Since we observe that Lorentz forces play a bigger role in the $E = 10^{-5}$ models, we suspect that magnetic feedback may be responsible for the changing nature of the morphology transition.

Regarding the breakdown of dipolar field generation, a leading hypothesis is that the dipolarity transition is controlled by the relative strengths of inertial and Coriolis forces (e.g., Christensen and Aubert, 2006). This is tested in Fig. 6c, which shows that the Coriolis force exceeds the inertial force by at least an order of magnitude across the dipolarity transition, irrespective of the Ekman number. The dominance of the Coriolis force in both dipolar and multipolar dynamos is consistent with the idea that the transition is controlled, instead, by the competition between second order forces.

In Section 5, we present an alternative hypothesis that viscosity plays an important role in producing helical flow, and therefore dipolar magnetic fields, in our $E = 10^{-4}$ models. We test this hypothesis for all of our models in Fig. 6d, which shows dipolarity plotted against the ratio of inertial to viscous force integrals. We find that the transition between dipole-dominated and multipolar dynamos occurs when the inertial and viscous forces become comparable. This result supports our hypothesis, which then suggests that viscous effects are important for dipolar field generation in many present day dynamo simulations.

We have shown that magnetic fields exert a stronger influence on helicity at lower Ekman numbers (Fig. 6b). This increase in magnetic field effects with decreased Ekman number also occurs for other convective properties, although to a lesser extent. Supplementary Table 6 gives the unsigned mean and maximum percent differences in the characteristics of convection between the dynamo and non-magnetic models for each E considered. These comparisons show that magnetic fields typically modify the convective properties ($\overline{k_u}$, $C_{\omega z}$, $|H_z^{rel}|$, Re_c, Nu) by about 10%, for models with $E \geq 10^{-4}$. In contrast, for models with $E = 10^{-5}$, the average percent difference increases to about 30% for typical flow length scales and columnarity and 50% for convective flow speeds and heat transfer efficiency.
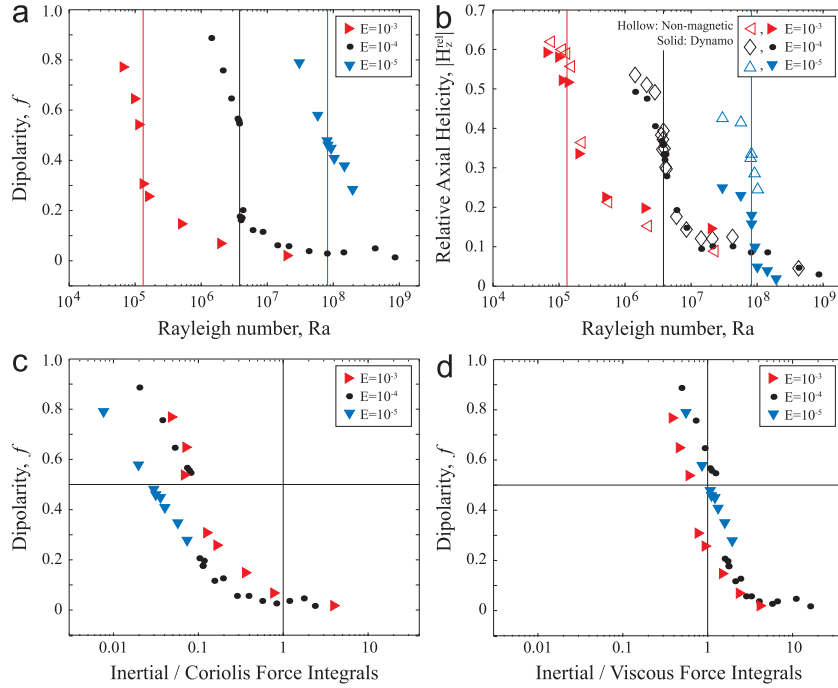
Fig. 6. (a) Time-averaged dipolarity, f, and (b) instantaneous relative axial helicity, $|H_z^{rel}|$, versus the Rayleigh number for all dynamo models, where vertical lines denote the transition between dipolar and multipolar dynamos (at $f = 0.5$). Hollow markers denote non-magnetic models in (b). Time-averaged dipolarity versus the instantaneous (c) inertial to Coriolis and (d) inertial to viscous force integral ratios. Here, horizontal lines indicate the dipolarity transition, while vertical lines indicate force integral ratios of unity.

Similar trends have also been reported in the literature. For example, Stellmach and Hansen (2004) show that the influence of magnetic fields on typical length scales of convection tends to increase with decreased E in Cartesian dynamo models. Sakuraba and Roberts (2009) also point out the possibility that Lorentz forces significantly affect dynamic length scales in low E models when thermal boundary conditions are changed.

The increasing impact of magnetic fields for lower E is captured by the calculated force integral ratios. While the Lorentz to Coriolis force ratios remain less than unity, the system appears to be trending toward magnetostrophic balance as the Ekman number is decreased for otherwise fixed control parameters. For example, when we fix $Ra = 1.9 Ra_c$ and $Pm = 2$, the Lorentz to Coriolis force integral ratios are $F_L/F_C = 0.15$ and $F_L/F_C = 0.29$ for models with $E = 10^{-4}$ and $E = 10^{-5}$, respectively.

Fig. 7 contrasts the calculated Λ_d values with the ratio of Lorentz to Coriolis force integrals for all of our models. The dynamic Elsasser number and the calculated force ratios typically differ by a factor of 1.5. (In contrast, the traditional Elsasser number tends to over-estimate the actual force ratio by an order of magnitude; see Supplementary Tables 4 and 5.) Thus, the dynamic Elsasser number provides an adequate estimate of the Lorentz to Coriolis force ratios for all of our planetary dynamo models.

7. Applications to planetary cores

Our results suggest that the dynamic Elsasser number, Λ_d, is a good indicator of the relative influence of magnetic fields on the field-generating flows. The difficulty in applying this parameter to planetary settings is its dependence on quantities that are poorly known: typical flow speeds and length scales of the magnetic field in the dynamo generation region. In order to extrapolate Λ_d to the low Ekman and magnetic Prandtl numbers appropriate for planetary interiors, a scaling law for the dynamic Elsasser number would be ideal. However, this is beyond the scope of the present work. Despite
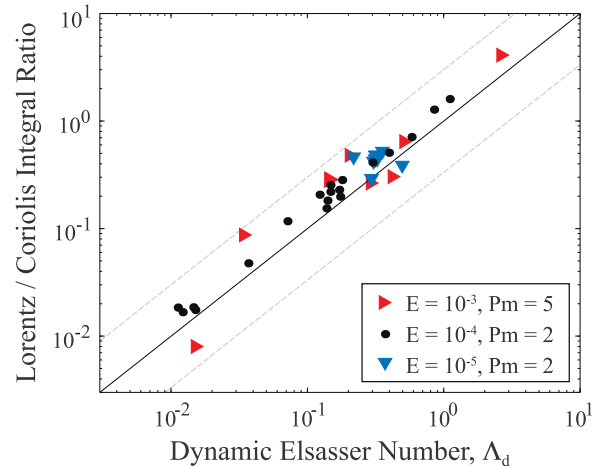
Fig. 7. Dynamic Elsasser numbers plotted against the Lorentz to Coriolis force integral ratios for all dynamo models. The solid black line indicates a one-to-one correlation, while the dashed gray lines indicate a factor of three difference.

this difficulty, we can make some simplifying assumptions to estimate the role of Lorentz forces in planetary dynamos.

Metallic planetary core fluids have small magnetic Prandtl numbers ($Pm \lesssim 10^{-5}$; e.g., Dobson et al., 2000). At such low Pm values, we can assume, as a first order estimate, that the magnetic field is predominantly large-scale ($\ell_B \sim D$). Then the dynamic Elsasser number in (17) can be written as

$$\Lambda_d = \frac{B^2}{2\mu_o \rho \Omega U D} = \frac{\Lambda_i}{Rm}. \tag{19}$$

Using estimates for planetary dynamo regions of $\Lambda_i \lesssim 1$ and $Rm \gtrsim 100$ (Schubert and Soderlund, 2011), all planets with active magnetic fields are predicted to have Λ_d values less than unity. Extrapolating our results to planetary settings, we therefore predict that convection motions, excluding axisymmetric zonal

flows, in planetary interiors are not strongly influenced by their *large-scale* magnetic fields. This is consistent with the analysis of geomagnetic secular variation data, which suggests that large-scale flows in Earth's core are quasigeostrophic (Schaeffer and Pais, 2011) and indicates that the Lorentz force is not strong enough to release the rotational constraint. However, the role of the Lorentz force due to smaller-scale field structures will depend on the high-order spatial spectrum of the field, which is not well known for any planet.

We have also hypothesized that the helical flow responsible for large-scale magnetic field generation in the $E \geq 10^{-4}$ simulations is viscously controlled. If true, it is unlikely that such models correctly reproduce the physical mechanisms of field generation in planetary cores where viscosity is thought to be negligible. Thus, we caution that moderate Ekman number models may operate in different dynamical regimes than planets.

8. Summary

We have carried out a broad survey of dynamo and non-magnetic rotating convection models in which the array of behaviors are mapped as a function of thermal forcing (Ra) and rotation rate (E^{-1}). Comparisons of dynamos against otherwise identical, non-magnetic models indicate that the characteristics of convection (axial vorticity isosurfaces, characteristic length scales, axial vorticity columnarity, relative axial helicity, convective flow speeds, heat transfer efficiency, and volume-integrated rms forces) are not significantly affected by magnetic fields in our models at moderate Ekman numbers ($E \geq 10^{-4}$). However, the Lorentz force can produce stronger changes in the $E = 10^{-5}$ models.

In addition, we calculate the mean amplitudes of the different forces, and show that the traditional Elsasser number, Λ_i, is not an appropriate measure of the relative strengths of the Lorentz and Coriolis forces. Instead, we argue that the dynamic Elsasser number, Λ_d, better parameterizes this ratio of forces. The over-estimation of the Lorentz force by Λ_i explains why columnar structures are maintained in many dynamo models (e.g., Olson and Glatzmaier, 1995; Zhang, 1995; Kageyama and Sato, 1997; Christensen et al., 1999; Zhang and Schubert, 2000; Jones, 2007; Jault, 2008), despite having magnetic fields with $\Lambda_i \gtrsim 1$. Further, extrapolating our results to planetary cores, we predict that the Lorentz force due to large-scale magnetic fields is weak compared to the Coriolis force in all planets with active dynamos.

We also observe pronounced dynamical regime transitions. In models with $E \geq 10^{-4}$, the collapse of dipolar magnetic fields coincides with the degradation of helical flow, which occurs even in the absence of magnetic fields and despite no significant change in columnarity. The comparison between dynamo and non-magnetic simulations suggests that the breakdown of dipolar field generation is largely a hydrodynamic process. Calculations of the hydrodynamic forces show that this transition occurs when the inertial and viscous forces become comparable. We hypothesize that helical flow is responsible for dipolar field generation, and that the role of viscous forces is essential for helical flow in these models.

In addition, our results indicate that the dynamics may be changing as the role of viscosity is decreased. Thus, dynamo models with moderate Ekman numbers $E \lesssim 10^{-4}$ may not correctly capture the physics of planetary dynamos, where viscosity is expected to be negligible.

Acknowledgments

Appendix A. Supplementary data

Supplementary data associated with this article can be found in the online version at http://dx.doi.org.10.1016/j.epsl.2012.03.038.

References

Aubert, J., 2005. Steady zonal flows in spherical shell dynamos. J. Fluid Mech. 542, 53–67.

Aubert, J., Aurnou, J.M., Wicht, J., 2008. The magnetic structure of convection-driven numerical dynamos. Geophys. J. Int. 172, 945–956.

Busse, F.H., Simitev, R.D., 2011. Remarks on some typical assumptions in dynamo theory. Geophys. Astrophys. Fluid Dyn. 105 (234–247).

Cardin, P., Brito, D., Jault, D., Nataf, H.C., Masson, J.P., 2002. Towards a rapidly rotating liquid sodium dynamo experiment. Magnetohydrodynamics 38, 177–189.

Cardin, P., Olson, P.L., 1995. The influence of toroidal magnetic field on thermal convection in the core. Earth Planet. Sci. Lett. 133, 167–181.

Castaing, B., Gunaratne, G., Heslot, F., Kadanoff, L., Libchaber, A., Thomae, S., Wu, X., Zaleski, S., Zanetti, G., 1989. Scaling of hard thermal turbulence in Rayleigh–Bénard convection. J. Fluid Mech. 204, 1–30.

Chandrasekhar, S., 1961. Hydrodynamic and Hydromagnetic Stability. Clarendon, Oxford.

Christensen, U.R., 2010. Dynamo scaling laws and applications to the planets. Space Sci. Rev. 152, 565–590.

Christensen, U.R., 2011. Geodynamo models: tools for understanding properties of Earth's magnetic field. Phys. Earth Planet. Int. 187, 157–169.

Christensen, U.R., Aubert, J., 2006. Scaling properties of convection driven dynamos in rotating spherical shells and application to planetary magnetic fields. Geophys. J. Int. 166, 97–114.

Christensen, U.R., Aubert, J., Hulot, G., 2010. Conditions for Earth-like geodynamo models. Earth Planet. Sci. Lett. 296, 487–496.

Christensen, U.R., Olson, P.L., Glatzmaier, G.A., 1999. Numerical modeling of the geodynamo: a systematic parameter study. Geophys. J. Int. 138, 393–409.

Christensen, U.R., Wicht, J., 2007. Numerical dynamo simulations. In: Olson, P.L. (Ed.), Treatise on Geophysics, vol. 8. Elsevier, pp. 245–282.

Connerney, J.E.P., 2007. Planetary magnetism. In: Spohn, T. (Ed.), Treatise on Geophysics, vol. 10. Elsevier, pp. 243–280.

Dobson, D.P., Crichton, W.A., Vocadlo, L., Jones, A.P., Wang, Y.B., Uchida, T., Rivers, M., Sutton, S., Brodholt, J.P., 2000. In situ measurements of viscosity of liquids in the Fe–FeS system at high pressures and temperatures. Am. Mineral. 85, 1838–1842.

Dormy, E., 2011. Stability and bifurcation of planetary dynamo models. J. Fluid Mech. 688, 1–4.

Dormy, E., Soward, A.M., Jones, C.A., Jault, D., Cardin, P., 2004. The onset of thermal convection in rotating spherical shells. J. Fluid Mech. 501, 43–70.

Eltayeb, I., Roberts, P.H., 1970. On the hydromagnetics of rotating fluids. Astrophys. J. 163, 699–701.

Fearn, D.R., Proctor, M.R.E., 1983. Hydromagnetic waves in a differentially rotating sphere. J. Fluid Mech. 128, 1–20.

Fearn, D.R., Roberts, P.H., Soward, A.M., 1988. Convection, stability, and the dynamo. In: Galdi, G.P., Straughan, B. (Eds.), Energy Stability and Convection. Longman Scientific Technical, Harlow, pp. 60–324.

Gaidos, E., Conrad, C.P., Manga, M., Hernlund, J., 2010. Thermodynamic limits on magnetodynamos in rocky exoplanets. Astrophys. J. 718, 596–607.

Gillet, N., Schaeffer, N., Jault, D., 2011. Rationale and geophysical evidence for quasi-geostrophic rapid dynamics within the Earth's outer core. Phys. Earth Planet. Int..

Glatzmaier, G.A., 1984. Numerical simulation of Stellar convective dynamos. I. The model and method. J. Comput. Phys. 55, 461–484.

Glazier, J., Segawa, T., Naert, A., Sano, M., 1999. Evidence against 'ultrahard' thermal turbulence at very high Rayleigh numbers. Nature 393, 307–310.

Grooms, I., Julien, K., Weiss, J.B., Knobloch, E., 2010. Model of convective Taylor columns in rotating Rayleigh–Bénard convection. Phys. Rev. Lett. 104, 224501.

Grote, E., Busse, F.H., 2001. Dynamics of convection and dynamos in rotating spherical fluid shells. Fluid Dyn. Res. 28, 349–368.

Jault, D., 2008. Axial invariance of rapidly varying diffusionless motions in the Earth's core interior. Phys. Earth Planet. Int. 166, 67–76.

Jones, C.A., 2007. Thermal and compositional convection in the outer core. In: Olson, P.L. (Ed.), Treatise on Geophysics, vol. 8. Elsevier, pp. 131–185.

Jones, C.A., 2011. Planetary magnetic fields and fluid dynamos. Annu. Rev. Fluid Mech. 43, 583–614.

Jones, C.A., Soward, A.M., Mussa, A.I., 2000. The onset of thermal convection in a rapidly rotating sphere. J. Fluid Mech. 405, 157–179.

Kageyama, A., Sato, T., 1997. Generation mechanism of a dipole field by a magnetohydrodynamic dynamo. Phys. Rev. E 55, 4617–4626.

King, E.M., Aurnou, J.M., 2012. Thermal evidence for Taylor columns in turbulent, rotating Rayleigh–Bénard convection. Phys. Rev. E 85, 016313.

King, E.M., Soderlund, K.M., Christensen, U.R., Wicht, J., Aurnou, J.M., 2010. Convective heat transfer in planetary dynamo models. Geochem. Geophys. Geosyst. 11, Q06016.

King, E.M., Stellmach, S., Noir, J., Hansen, U., Aurnou, J.M., 2009. Boundary layer control of rotating convection systems. Nature 457, 301–304.

Lehnert, B., 1954. Magnetohydrodynamic waves under the action of the Coriolis force. Astrophys. J. 119, 647–654.

Moffatt, H.K., 1978. Magnetic Field Generation in Electrically Conducting Fluids. Cambridge University Press, Cambridge.

Olson, P.L., 2011. Laboratory experiments on the dynamics of the core. Phys. Earth Planet. Int. 187, 139–156.

Olson, P.L., Christensen, U.R., 2006. Dipole moment scaling for convection-driven planetary dynamos. Earth Planet. Sci. Lett. 250, 561–571.

Olson, P.L., Christensen, U.R., Glatzmaier, G.A., 1999. Numerical modeling of the geodynamo: mechanisms of field generation and equilibration. J. Geophys. Res. 104, 10383–10404.

Olson, P.L., Glatzmaier, G.A., 1995. Magnetoconvection in a rotating spherical shell: structure of flow in the outer core. Phys. Earth Planet. Int. 92, 109–118.

Parker, E.N., 1955. Hydromagnetic dynamo models. Astrophys. J. 122, 293–314.

Roberts, P.H., 1968. On the thermal instability of a rotating-fluid sphere containing heat sources. Philos. Trans. R. Soc. London Ser. A 264, 93–117.

Roberts, P.H., 2007. Theory of the geodynamo. In: Olson, P.L. (Ed.), Treatise on Geophysics, vol. 8. Elsevier, pp. 67–105.

Roberts, P.H., Aurnou, J.M., 2011. On the theory of core–mantle coupling. Geophys. Astrophys. Fluid Dyn. 106, 157–230, http://dx.doi.org/10.1080/03091929.2011. 589028.

Sakuraba, M., Roberts, P.H., 2009. Generation of a strong magnetic field using uniform heat flux at the surface of the core. Nat. Geosci. 2, 802–805.

Sano, M., Wu, X.Z., Libchaber, A., 1989. Turbulence in helium-gas free convection. Phys. Rev. A 40, 6421–6430.

Schaeffer, N., Pais, M.A., 2011. On symmetry and anisotropy of Earth-core flows. Geophys. Res. Lett. 38, L10309, http://dx.doi.org/10.1029/2011GL046888.

Schmitz, S., Tilgner, A., 2010. Transitions in turbulent rotating Rayleigh–Bénard convection. Geophys. Astrophys. Fluid Dyn. 104, 481–489.

Schubert, G., Soderlund, K.M., 2011. Planetary magnetic fields: observations and models. Phys. Earth Planet. Int. 187, 92–108.

Siggia, E.D., 1994. High Rayleigh number convection. Annu. Rev. Fluid Mech. 26, 137–168.

Simitev, R.D., Busse, F.H., 2009. Bistability and hysteresis of dipolar dynamos generated by turbulent convection in rotating spherical shells. Europhys. Lett. 85, 19001.

Sreenivasan, B., Jones, C.A., 2006. The role of inertia in the evolution of spherical dynamos. Geophys. J. Int. 164, 467–476.

Sreenivasan, B., Jones, C.A., 2011. Helicity generation and subcritical behavior in rapidly rotating dynamos. J. Fluid Mech. 688, 5–30.

Stellmach, S., Hansen, U., 2004. Cartesian convection driven dynamos at low Ekman number. Phys. Rev. E 70, 056312.

Tilgner, A., 1996. High Rayleigh number convection in spherical shells. Phys. Rev. E 53, 4847–4851.

Tritton, D.J., 1998. Physical Fluid Dynamics. Oxford University Press, Oxford.

Wicht, J., 2002. Inner-core conductivity in numerical dynamo simulations. Phys. Earth Planet. Int. 132, 281–302.

Zhang, K., 1995. Spherical shell rotating convection in the presence of toroidal magnetic field. Proc. R. Soc. London A 448, 245–268.

Zhang, K., Jones, C.A., Sarson, G.R., 1998. The dynamical effects of hyperviscosity on numerical geodynamo models. Stud. Geophys. Geod. 22, 1265–1268.

Zhang, K., Schubert, G., 2000. Magnetohydrodynamics in rapidly rotating spherical systems. Annu. Rev. Fluid Mech. 32, 409–443.

Ra	$\frac{Ra}{Ra_c}$	N_{ro}	l_{max}	Nu	Re_c	Re	$C_{\omega z}$	$|H_z^{rel}|$	$\overline{k_u}$	$\overline{k_B}$	f	Λ_i	Λ_d	λ	$\frac{F_L}{F_C}$	$\frac{F_I}{F_V}$
1.42×10^6	1.9	41	64	1.88	32	34	0.69	0.49	15.0	11.6	0.89	1.31	0.14	0.06	0.15	0.49
				(1.74)	(41)	(43)	(0.70)	(0.54)	(17.5)							(0.72)
2.12×10^6	2.8	41	64	2.54	51	52	0.66	0.48	17.3	13.6	0.76	2.10	0.18	0.09	0.20	0.72
				(2.32)	(64)	(67)	(0.67)	(0.51)	(19.7)							(1.15)
2.83×10^6	3.8	41	64	3.19	70	72	0.60	0.41	18.6	15.8	0.65	2.42	0.17	0.11	0.22	0.92
				(2.98)	(89)	(92)	(0.63)	(0.49)	(19.4)							(1.30)
3.54×10^6	4.7	41	64	3.78	90	91	0.60	0.37	19.5	18.1	0.57	2.37	0.15	0.13	0.25	1.06
				(3.74)	(113)	(118)	(0.60)	(0.38)	(18.9)							(1.64)
3.68×10^6	4.9	41	64	3.88	93	95	0.60	0.36	19.6	18.7	0.56	2.36	0.15	0.13	0.23	1.11
				(3.88)	(117)	(123)	(0.61)	(0.35)	(18.9)							(1.67)
3.75×10^6	5.0	41	64	3.94	96	98	0.61	0.35	19.7	18.9	0.55	2.27	0.14	0.13	0.18	1.23
				(3.94)	(119)	(125)	(0.63)	(0.37)	(18.8)							(1.70)
3.82×10^6	5.1	41	64	4.03	119	124	0.63	0.37	19.1	26.9	0.21	0.14	0.01	0.05	0.02	1.58
				(4.00)	(121)	(127)	(0.61)	(0.39)	(18.8)							(1.73)
3.96×10^6	5.3	41	64	4.15	123	128	0.59	0.33	19.1	26.7	0.18	0.18	0.01	0.05	0.02	1.75
				(4.13)	(126)	(132)	(0.61)	(0.35)	(18.7)							(1.80)
4.11×10^6	5.5	41	64	4.28	127	131	0.59	0.33	19.0	26.8	0.18	0.22	0.01	0.06	0.02	1.76
				(4.25)	(130)	(136)	(0.59)	(0.30)	(18.7)							(1.90)
4.24×10^6	5.6	41	85	4.38	130	135	0.60	0.28	19.0	27.2	0.20	0.24	0.02	0.06	0.02	1.71
				(4.36)	(133)	(140)	(0.58)	(0.30)	(18.6)							(1.85)
6.00×10^6	8.0	41	85	5.57	169	174	0.57	0.19	19.2	29.0	0.12	0.68	0.04	0.11	0.05	2.10
				(5.57)	(179)	(188)	(0.55)	(0.18)	(18.1)							(2.24)
8.50×10^6	11	41	128	6.72	210	216	0.54	0.15	19.1	31.4	0.13	1.53	0.07	0.18	0.12	2.42
				(6.77)	(231)	(246)	(0.52)	(0.14)	(17.7)							(2.97)
1.42×10^7	19	49	128	8.39	285	295	0.45	0.10	18.7	34.6	0.06	3.44	0.13	0.29	0.20	2.82
				(8.52)	(326)	(353)	(0.43)	(0.12)	(17.2)							(3.74)
2.10×10^7	28	49	128	9.73	357	368	0.40	0.10	18.6	37.8	0.06	5.49	0.18	0.40	0.28	3.24
				(9.91)	(417)	(453)	(0.41)	(0.12)	(17.0)							(4.46)
$*2.10 \times 10^7$	28	49	128	9.71	352	358	0.43	0.07	15.6	22.7	0.08	7.56	0.15	0.40	0.07	4.45
4.24×10^7	56	49	192	12.4	540	557	0.34	0.10	17.3	44.9	0.04	11.4	0.29	0.68	0.41	4.00
				(12.7)	(652)	(686)	(0.31)	(0.13)	(17.4)							(5.71)
8.00×10^7	106	49	192	15.2	821	846	0.29	0.09	15.7	51.0	0.03	20.7	0.40	1.04	0.51	5.71
1.42×10^8	188	65	192	17.8	1116	1156	0.26	0.09	14.5	58.1	0.04	36.3	0.58	1.58	0.70	6.56
$*4.24 \times 10^8$	562	65	192	23.4	1790	2014	0.26	0.05	12.5	50.5	0.05	106	0.85	2.34	1.27	10.9
$*$				(25.0)	(2139)	(2470)	(0.23)	(0.05)	(13.7)							(18.3)
$*8.48 \times 10^8$	1125	65	192	27.0	2281	2618	0.24	0.03	13.2	46.3	0.02	197	1.11	2.92	1.60	16.1

Table 4: Input and output parameters for fixed $\chi = 0.4$, $Pr = 1$, $Pm = 2$, and $E = 10^{-4}$. Non-magnetic values are given in parentheses. All output quantities are time-averaged, except for $C_{\omega z}$, $|H_z^{rel}|$, F_L/F_C, and F_I/F_V. The number of radial grid points in the outer and inner cores is denoted N_{ro} and $N_{ri} = 17$, respectively. All other parameters are defined in Table 1 and 2. Asterisks indicate the use of hyperdiffusion (see Table 3). Dynamo models have dipolar (multipolar) magnetic fields above (below) the short-dashed line and columnar (3D) convection above (below) the long-dashed line.

Ra	$\frac{Ra}{Ra_c}$	N_{ro}	l_{max}	Nu	Re_c	Re	$C_{\omega z}$	$|H_z^{rel}|$	$\overline{k_u}$	$\overline{k_B}$	f	Λ_i	Λ_d	λ	$\frac{F_L}{F_C}$	$\frac{F_I}{F_V}$
$E = 10^{-3},\ \ Pm = 5$																
6.40×10^4	1.9	37	42	1.45	10	10	0.74	0.59	7.1	7.9	0.77	1.74	0.42	0.21	0.30	0.38
				(1.43)	(13)	(13)	(0.73)	(0.62)	(9.7)							(0.44)
9.70×10^4	2.8	37	42	1.60	14	15	0.67	0.58	8.5	8.9	0.65	1.56	0.30	0.22	0.26	0.46
				(1.71)	(19)	(20)	(0.67)	(0.60)	(10.6)							(0.60)
1.12×10^5	3.2	37	42	1.80	19	20	0.70	0.54	8.6	9.7	0.54	1.30	0.20	0.22	0.18	0.60
				(1.83)	(22)	(23)	(0.67)	(0.59)	(10.6)							(0.67)
1.32×10^5	3.8	37	42	2.02	27	27	0.66	0.52	9.4	11.8	0.31	0.24	0.03	0.12	0.09	0.77
				(1.97)	(26)	(27)	(0.65)	(0.56)	(9.8)							(0.82)
1.60×10^5	4.6	37	42	2.16	31	32	0.64	0.47	9.5	13.4	0.26	0.11	0.02	0.09	0.01	0.92
				(2.15)	(31)	(32)	(0.64)	(0.48)	(9.5)							(0.90)
5.00×10^6	14	37	64	3.55	69	70	0.53	0.23	9.4	19.7	0.15	1.62	0.14	0.50	0.28	1.47
				(3.59)	(73)	(75)	(0.55)	(0.21)	(9.7)							(1.77)
1.96×10^6	56	37	64	5.45	143	151	0.41	0.16	9.6	26.3	0.07	9.11	0.50	1.60	0.64	2.34
				(5.60)	(163)	(176)	(0.39)	(0.15)	(9.3)							(3.17)
1.96×10^7	560	37	64	10.7	419	454	0.24	0.10	12.7	37.7	0.02	99.2	2.62	7.57	4.10	4.07
				(11.3)	(526)	(565)	(0.25)	(0.09)	(13.1)							(5.95)
$E = 10^{-5},\ \ Pm = 2$																
3.10×10^7	1.9	49	128	3.07	75	78	0.56	0.25	23.1	15.2	0.79	4.84	0.30	0.07	0.29	0.55
				(2.08)	(122)	(127)	(0.70)	(0.43)	(34.9)							(1.29)
5.89×10^7	3.7	49	192	5.09	153	158	0.46	0.23	29.7	22.0	0.58	7.07	0.31	0.12	0.42	0.87
				(4.02)	(271)	(284)	(0.63)	(0.42)	(34.0)							(2.29)
8.20×10^7	5.0	49	192	6.70	214	221	0.45	0.18	33.3	27.0	0.48	8.39	0.32	0.16	0.44	1.07
				(6.15)	(407)	(436)	(0.60)	(0.33)	(30.5)							(3.11)
8.50×10^7	5.2	49	192	7.04	227	235	0.46	0.16	32.9	27.7	0.46	8.82	0.33	0.17	0.44	1.12
				(6.45)	(420)	(454)	(0.60)	(0.34)	(30.5)							(3.21)
9.50×10^7	5.8	49	192	7.28	248	257	0.44	0.10	33.8	29.2	0.45	8.85	0.32	0.17	0.48	1.20
				(7.29)	(474)	(514)	(0.59)	(0.29)	(29.5)							(3.63)
1.05×10^8	6.5	49	192	8.10	279	289	0.43	0.05	35.9	31.2	0.41	9.37	0.32	0.19	0.44	1.34
				(8.17)	(524)	(570)	(0.58)	(0.25)	(29.2)							(3.94)
1.50×10^8	9.2	65	213	9.85	364	377	0.40	0.04	36.5	34.9	0.35	12.4	0.36	0.25	0.52	1.61
$*2.00 \times 10^8$	12.5	65	213	12.2	466	480	0.42	0.02	36.7	38.6	0.28	14.6	0.38	0.30	0.52	1.95

Table 5: Input and output parameters for fixed $\chi = 0.4$ and $Pr = 1$. Non-magnetic values are given in parentheses. All output quantities are time-averaged, except for $C_{\omega z}$, $|H_z^{rel}|$, F_L/F_C, and F_I/F_V. The number of radial grid points in the outer and inner cores is denoted N_{ro} and $N_{ri} = 17$, respectively. All other parameters are defined in Tables 1 and 2. Asterisks indicate the use of hyperdiffusion (see Table 3). For each Ekman number, the short-dashed horizontal line indicates the breakdown of dipolar magnetic field generation.

	$E = 10^{-3}$	$E = 10^{-4}$	$E = 10^{-5}$
Characteristic degree of the flow, $\overline{k_u}$	10 (27)	6 (14)	17 (34)
Columnarity, $C_{\omega z}$	2 (6)	4 (14)	24 (27)
Relative axial helicity, $|H_z^{rel}|$	7 (13)	10 (22)	55 (80)
Convective flow speed, Re_c	13 (26)	13 (21)	45 (48)
Heat transfer efficiency, Nu	3 (6)	3 (10)	16 (48)

Table 6: Unsigned mean (maximum) percent differences of convective properties between the dynamo and non-magnetic values for all Ekman numbers investigated. All parameters are defined in Table 2.

Corrigendum

Corrigendum to "The influence of magnetic fields in planetary dynamo models" [Earth Planet. Sci. Lett. 333–334 (2012) 9–20]

K.M. Soderlund [a,*], E.M. King [b], J.M. Aurnou [c]

[a] *Institute for Geophysics, Jackson School of Geosciences, University of Texas at Austin, Austin, TX 78758, USA*
[b] *Department of Earth and Planetary Science, University of California, Berkeley, CA 94720, USA*
[c] *Department of Earth, Planetary, and Space Sciences, University of California, Los Angeles, CA 90095, USA*

A R T I C L E   I N F O

Article history:
Available online xxxx

We have investigated the influence of magnetic fields on the convective properties of planetary dynamo models and the transition between dynamos with dipolar and multipolar magnetic fields in Soderlund et al. (2012). We thank Uli Christensen for pointing out an error solely in our algorithm used to calculate the volumetric average of relative axial helicity, H_z^{rel}. However, it should be noted that the main results of the paper remain intact, as discussed below.

Relative axial helicity is defined as axial helicity normalized by its maximum possible value,

$$H_z^{rel} = \frac{\langle u_z \omega_z \rangle_h}{(\langle u_z u_z \rangle_h \langle \omega_z \omega_z \rangle_h)^{1/2}}, \qquad (1)$$

where u_z is axial velocity, $\omega_z = \nabla \times \mathbf{u} \cdot \hat{\mathbf{z}}$ is axial vorticity, and $\langle\rangle_h$ is the volumetric average in each hemisphere excluding boundary layers (e.g., Olson et al., 1999; Schmitz and Tilgner, 2010). We average the helicity magnitude over each hemisphere since axial helicity tends to be anti-symmetric across the equator and assume Ekman boundary layer thicknesses of $\delta_E/D = 3E^{1/2}$ following King et al. (2012).

In Soderlund et al. (2012), the $|H_z^{rel}|$ calculations are missing a factor of $\sin\theta$ in the volume integral. The erroneously calculated helicity data are shown in Fig. 1a. The effect of this missing factor is to weight the contributions within the tangent cylinder too heavily.

Corrected $|H_z^{rel}|$ are shown in Fig. 1b. While instantaneous values were given in Soderlund et al. (2012), here we report the average of three random snapshots in time for each case. Temporal

standard deviations (σ) are typically near 0.02. The corrected values differ on average from the original values by [0.02 (0.02), 0.04 (0.04), 0.07 (0.02)] for cases with $E = [10^{-3}, 10^{-4}, 10^{-5}]$ where parentheses indicate non-magnetic cases. These differences only exceed 2σ in the lowest Ekman number dynamo cases.

Tables 1 and 2 provide corrected values of $|H_z^{rel}|$. In addition, we have also included time averaged values of axial vorticity columnarity $C_{\omega z}$, in situ Lorentz to Coriolis force ratio F_L/F_C, and in situ inertial to viscous force ratio F_I/F_V.

The two main conclusions of the paper are not modified significantly. They are: (i) The magnetic fields do not strongly affect relative axial helicity in cases with $E \geqslant 10^{-4}$. This weak influence can be understood theoretically by estimating the strength of the Lorentz forces in the high magnetic Reynolds number limit with a dynamic Elsasser number, $\Lambda_d = B^2/(2\rho\mu_o\Omega U \ell_B)$. Calculations of the dynamic Elsasser number correctly capture the secondary influence of Lorentz forces on convection. (ii) The breakdown of dipolar magnetic field generation still coincides with the degradation of helicity in the flow, even though the helicity decreases are markedly less abrupt than originally reported (see Fig. 1b). Importantly, the dipolarity breakdown still occurs when the inertial and viscous forces become comparable, $F_I/F_V \sim 1$, for all Ekman numbers considered here ($10^{-3} \geqslant E \geqslant 10^{-5}$). Because viscosity is expected to be negligible in planetary settings, the dipolarity breakdown in present day dynamo models with moderate Ekman numbers may not extrapolate to planets.

Acknowledgements

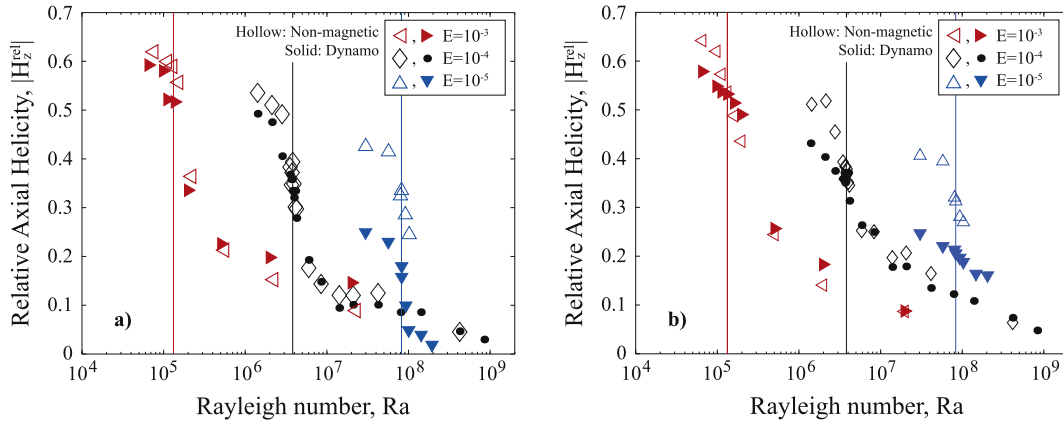DOI of original article: http://dx.doi.org/10.1016/j.epsl.2012.03.038.

* Corresponding author. Tel.: +1 (218) 349 3006; fax: +1 (512) 471 8844.
E-mail addresses: krista@ig.utexas.edu (K.M. Soderlund), eric.king@berkeley.edu (E.M. King), aurnou@ucla.edu (J.M. Aurnou).

Fig. 1. (a) Instantaneous relative axial helicity, $|H_z^{rel}|$, versus the Rayleigh number published in Soderlund et al. (2012). (b) Corrected relative axial helicity, $|H_z^{rel}|$, versus the Rayleigh number using the average of three random snapshots in time. The temporal standard deviations are typically ∼0.02; errorbars are not included for clarity. Vertical lines denote the transition between dipolar and multipolar dynamos (at $f = 0.5$). Filled (hollow) markers denote dynamo (non-magnetic) models.

Table 1
Input and time-averaged output parameters for fixed $\chi = 0.4$, $Pr = 1$, $Pm = 2$, and $E = 10^{-4}$. Non-magnetic values are given in parentheses. The average of three random snapshots in time are used to calculate $C_{\omega z}$, $|H_z^{rel}|$, F_L/F_C, and F_I/F_V; single snapshots were used in Soderlund et al. (2012). All parameters are defined in Tables 1 and 2 of Soderlund et al. (2012). Asterisks indicate the use of hyperdiffusion.

Ra	$\frac{Ra}{Ra_c}$	N_{ro}	l_{max}	Nu	Re_c	Re	$C_{\omega z}$	$|H_z^{rel}|$	$\bar{k_u}$	$\bar{k_B}$	f	Λ_i	Λ_d	λ	$\frac{F_L}{F_C}$	$\frac{F_L}{F_V}$
1.42×10^6	1.9	41	64	1.88	33	34	0.70	0.43	15.0	11.6	0.89	1.30	0.14	0.06	0.18	0.44
				(1.74)	(41)	(43)	(0.70)	(0.51)	(17.4)							(0.67)
2.12×10^6	2.8	41	64	2.55	51	52	0.63	0.40	17.2	13.6	0.76	2.10	0.17	0.09	0.21	0.68
				(2.32)	(64)	(67)	(0.63)	(0.52)	(19.6)							(0.94)
2.83×10^6	3.8	41	64	3.19	70	72	0.57	0.38	18.6	15.8	0.65	2.42	0.17	0.11	0.24	0.83
				(2.98)	(89)	(92)	(0.62)	(0.46)	(19.4)							(1.25)
3.54×10^6	4.7	41	64	3.78	89	91	0.55	0.36	19.5	18.0	0.57	2.37	0.15	0.12	0.27	1.01
				(3.74)	(113)	(118)	(0.60)	(0.39)	(18.9)							(1.62)
3.68×10^6	4.9	41	64	3.88	93	95	0.56	0.37	19.6	18.6	0.56	2.36	0.15	0.13	0.21	1.04
				(3.88)	(117)	(123)	(0.60)	(0.36)	(18.8)							(1.56)
3.75×10^6	5.0	41	64	3.94	96	98	0.58	0.35	19.7	18.9	0.55	2.27	0.14	0.13	0.21	1.11
				(3.94)	(119)	(125)	(0.59)	(0.38)	(18.8)							(1.60)
3.82×10^6	5.1	41	64	4.04	120	124	0.58	0.35	18.9	26.7	0.18	0.14	0.01	0.05	0.01	1.50
				(4.00)	(121)	(127)	(0.59)	(0.38)	(18.8)							(1.63)
3.96×10^6	5.3	41	64	4.15	123	128	0.59	0.37	19.0	26.6	0.16	0.18	0.01	0.05	0.02	1.56
				(4.13)	(126)	(132)	(0.59)	(0.38)	(18.7)							(1.67)
4.11×10^6	5.5	41	64	4.28	127	131	0.57	0.37	19.0	26.8	0.17	0.22	0.01	0.06	0.02	1.61
				(4.26)	(130)	(136)	(0.58)	(0.35)	(18.6)							(1.72)
4.24×10^6	5.6	41	85	4.38	130	135	0.59	0.31	19.0	27.1	0.20	0.24	0.02	0.06	0.02	1.60
				(4.36)	(133)	(140)	(0.57)	(0.35)	(18.6)							(1.75)
6.00×10^6	8.0	41	85	5.57	169	174	0.54	0.26	19.1	29.0	0.12	0.68	0.04	0.11	0.06	1.96
				(5.57)	(179)	(188)	(0.55)	(0.25)	(18.0)							(2.15)
8.50×10^6	11	41	128	6.72	210	216	0.50	0.25	19.0	31.4	0.12	1.53	0.07	0.17	0.11	2.27
				(6.77)	(231)	(246)	(0.49)	(0.25)	(17.7)							(2.79)
1.42×10^7	19	49	128	8.41	285	293	0.43	0.18	18.7	34.6	0.06	3.44	0.13	0.29	0.21	2.76
				(8.53)	(326)	(353)	(0.43)	(0.20)	(17.2)							(3.37)
2.10×10^7	28	49	128	9.73	357	368	0.37	0.18	18.6	37.8	0.06	5.48	0.18	0.40	0.28	3.09
				(9.91)	(417)	(453)	(0.36)	(0.21)	(17.0)							(4.26)
$2.10 \times 10^{7*}$	28	49	128	9.70	350	358	0.43	0.17	15.5	22.7	0.08	7.61	0.15	0.28	0.25	3.81
4.24×10^7	56	49	192	12.4	540	557	0.28	0.14	17.3	44.9	0.04	11.4	0.29	0.68	0.44	4.21
				(12.7)	(647)	(684)	(0.28)	(0.17)	(17.4)							(5.70)
8.00×10^7	106	49	192	15.1	820	845	0.24	0.12	15.6	51.0	0.03	20.7	0.40	1.05	0.59	5.38
1.42×10^8	188	65	192	17.8	1117	1153	0.22	0.11	14.5	58.0	0.04	36.3	0.58	1.57	0.81	6.65
$4.24 \times 10^{8*}$	562	65	192	23.4	1802	2017	0.19	0.07	12.5	50.5	0.05	106	0.84	2.34	1.18	11.8
				(24.9)	(2139)	(2472)	(0.18)	(0.06)	(13.7)							(16.9)
$8.48 \times 10^{8*}$	1125	65	192	27.0	2281	2613	0.18	0.05	13.2	46.3	0.02	197	1.11	2.92	1.63	16.3

Table 2

Input and time-averaged output parameters for fixed $\chi = 0.4$ and $Pr = 1$ using the notation of Table 1. Two dynamos with $E = 10^{-3}$ were found to decay with additional runtime.

Ra	$\frac{Ra}{Ra_c}$	N_{ro}	l_{max}	Nu	Re_c	Re	$C_{\omega z}$	$|H_z^{rel}|$	$\overline{k_u}$	$\overline{k_B}$	f	Λ_i	Λ_d	λ	$\frac{F_L}{F_C}$	$\frac{F_L}{F_V}$
$E = 10^{-3}$, $Pm = 5$																
6.50×10^4	1.9	37	42	1.45	10	10	0.76	0.58	7.1	7.9	0.78	4.34	0.42	0.15	0.39	0.33
				(1.43)	(13)	(13)	(0.75)	(0.64)	(9.7)							(0.39)
9.70×10^4	2.8	37	42	1.60	14	15	0.69	0.55	8.5	8.9	0.65	3.91	0.30	0.16	0.43	0.40
				(1.71)	(19)	(20)	(0.71)	(0.62)	(10.6)							(0.57)
1.12×10^5	3.2	37	42	1.80	19	20	0.70	0.54	8.6	9.7	0.54	3.25	0.20	0.16	0.40	0.48
				(1.82)	(22)	(23)	(0.71)	(0.57)	(10.6)							(0.64)
1.32×10^5	3.8	37	42	2.02	27	27	0.71	0.53	9.4	11.8	0.31	0.61	0.03	0.08	0.05	0.75
				(1.97)	(26)	(27)	(0.70)	(0.54)	(9.8)							(0.73)
1.60×10^5	4.6	37	42	2.16	31	31	0.68	0.51	9.7	–	–	$\to 0$	$\to 0$	$\to 0$	$\to 0$	0.90
				(2.16)	(31)	(32)	(0.66)	(0.49)	(9.8)							(0.84)
1.96×10^5	5.6	37	42	2.38	36	37	0.64	0.49	9.9	–	–	$\to 0$	$\to 0$	$\to 0$	$\to 0$	0.95
				(2.40)	(36)	(37)	(0.63)	(0.44)	(9.9)							(0.92)
5.00×10^5	14	37	64	3.55	69	70	0.52	0.26	9.4	19.6	0.14	4.14	0.15	0.36	0.29	1.39
				(3.59)	(74)	(75)	(0.49)	(0.24)	(9.5)							(1.72)
1.96×10^6	56	37	64	5.45	143	151	0.38	0.18	9.6	26.3	0.07	23.0	0.51	1.13	0.79	2.22
				(5.60)	(163)	(176)	(0.34)	(0.14)	(9.3)							(3.16)
1.96×10^7	560	37	64	10.7	419	454	0.23	0.09	12.7	37.7	0.02	248	2.62	5.35	4.20	3.68
				(11.3)	(526)	(565)	(0.21)	(0.09)	(13.1)							(5.54)
$E = 10^{-5}$, $Pm = 2$																
3.10×10^7	1.9	49	128	3.07	75	78	0.48	0.25	23.1	15.2	0.79	4.84	0.30	0.05	0.39	0.42
				(2.08)	(122)	(127)	(0.66)	(0.41)	(34.9)							(0.99)
5.89×10^7	3.6	49	170	5.09	153	159	0.42	0.22	29.7	22.0	0.58	7.07	0.31	0.08	0.45	0.71
				(4.01)	(271)	(284)	(0.60)	(0.39)	(33.9)							(1.95)
8.20×10^7	5.0	49	192	6.73	218	225	0.42	0.21	33.2	27.0	0.48	8.28	0.32	0.11	0.45	0.97
				(6.15)	(407)	(436)	(0.58)	(0.32)	(30.5)							(2.76)
8.50×10^7	5.2	49	192	6.81	224	231	0.40	0.19	32.9	27.4	0.47	8.54	0.32	0.11	0.47	0.96
				(6.45)	(420)	(454)	(0.57)	(0.31)	(30.5)							(2.89)
9.50×10^7	5.8	49	192	7.41	251	259	0.41	0.20	34.1	29.2	0.45	9.02	0.32	0.12	0.45	1.12
				(7.29)	(474)	(512)	(0.56)	(0.28)	(29.6)							(3.26)
1.05×10^8	6.5	49	192	8.03	274	283	0.40	0.19	35.5	30.7	0.42	9.63	0.33	0.14	0.47	1.17
				(8.17)	(524)	(570)	(0.55)	(0.27)	(29.2)							(3.59)
1.50×10^8	9.2	65	213	9.98	363	374	0.37	0.16	35.9	34.2	0.37	12.4	0.36	0.17	0.52	1.49
$2.00 \times 10^{8*}$	12.3	65	213	12.3	470	483	0.36	0.16	37.1	39.0	0.29	14.8	0.38	0.21	0.56	1.83

References

King, E.M., Stellmach, S., Aurnou, J.M., 2012. Heat transfer by rapidly rotating Rayleigh–Bénard convection. J. Fluid Mech. 691, 568–582.

Olson, P.L., Christensen, U.R., Glatzmaier, G.A., 1999. Numerical modeling of the geodynamo: Mechanisms of field generation and equilibration. J. Geophys. Res. 104, 10383–10404.

Schmitz, S., Tilgner, A., 2010. Transitions in turbulent rotating Rayleigh–Bènard convection. Geophys. Astrophys. Fluid Dyn. 104, 481–489.

Soderlund, K.M., King, E.M., Aurnou, J.M., 2012. The influence of magnetic fields in planetary dynamo models. Earth Planet. Sci. Lett. 333–334, 9–20.